

<https://journals.sagepub.com/home/pin>

Accepted May 13th 2025

Computation of unsteady reactive magnetized bioconvective micropolar nanofluid squeezing flow with Stefan blowing and heat source effects

O. Anwar Bég¹, W.A. Khan², Shakil Mojumdar³, M.J. Uddin^{3} and T. A. Bég⁴*

¹*MPESG, Corrosion/Coating Lab, 3-08, Aeronautical & Mechanical Engineering Dept., SEE Building, Salford University, Manchester, M54WT, UK., Email- O.A.Beg@salford.ac.uk*

²*Department of Pure and Applied Mathematics, Saveetha School of Engineering. Saveetha Nagar, Thandalam, Chennai-602105, Tamilnadu, India.*

³*American International University-Bangladesh, 408/1, Kuratoli, Khilkhet, Dhaka 1229, Bangladesh, skmojumdar@aiub.edu; drjashim@aiub.edu*

⁴*Engineering Mechanics Research, Israfil House, Manchester, M13, UK. Email: tasveerabeg@gmail.com*

**Corresponding author: drjashim@aiub.edu*

ABSTRACT

Motivated by emerging applications in smart bio-nano-tribology, a mathematical model for the unsteady, magnetohydrodynamic chemically reacting bioconvective micropolar Buongiorno nanofluid squeezing flow between two parallel plates subject to Stefan blowing and heat source effects is developed, and examined. The presence of the gyrotactic bioconvection microorganisms in the nanofluid prevents nanoparticle agglomeration, improves the stability of nanofluids, improves mixing, and encourages the development of a beneficial nanoparticle volume fraction gradient. Suitable coordinate transformations are applied to reduce the fundamental transport equations into similarity equations before solving them numerically with a 4th-5th order Runge-Kutta Method within **Maple 24** symbolic software. The influences of the controlling parameters on the dimensionless velocity, angular velocity (micro-rotation), temperature, nanoparticle volume fraction (NPVF), density of motile microorganisms, as well as on the physical quantities (shear stress, Nusselt number, nanoparticle Sherwood number, and micro-organism density gradient) are investigated and visualized graphically. The computed results for the Nusselt number and NPVF Sherwood numbers are compared with existing results for several limiting cases, and excellent agreement is found. It is shown that skin friction increases with elevation in micro-rotation and blowing parameters, whereas Nusselt number, nanoparticle Sherwood number, and microorganism wall gradient increase with micro-rotation parameters both in the presence and absence of blowing. With increasing squeeze number, angular velocity, temperature, and NPVF increase substantially, whereas the motile microorganism density number weakly increases in the regime. Nusselt number is strongly enhanced with more significant magnetic field parameters, whereas it is reduced with larger values of micro-rotation parameter and squeeze number. The present study is relevant to hybrid magnetic lubrication systems and highlights the benefits of combining magnetic non-Newtonian nanofluids with bioconvection effects for improved thermal management.

KEYWORDS: *Squeezing flow; magnetic lubrication; bioconvection; micropolar nanofluid; Stefan blowing; Microorganisms; Maple 24.*

NOMENCLATURE

\tilde{b}	chemotaxis constant (m)
B	micro-inertia density parameter (-).
B^*	variable magnetic field strength (Tesla)
B_0^*	constant magnetic field strength (Tesla)
C	nanoparticle volume fraction (-)
C_1	lower plate nanoparticle volume fraction (-)
C_2	upper plate nanoparticle volume fraction (-)
C_f	local skin friction coefficient (-)
C_p	specific heat at constant pressure (J / KgK -)
D_B	Brownian diffusion coefficient (m^2s^{-1})
D_T	thermophoretic diffusion coefficient (m^2s^{-1})
D_n	microorganism diffusion coefficient (m^2s^{-1})
$f(\eta)$	dimensionless stream function (-)
s	blowing parameter (-)
$h(t)$	variable film thickness (m)
j	micro-inertia density (m^2)
K	micro-rotation (vortex viscosity) parameter (-)
k_1	micropolar vortex viscosity coefficient ($kgm^{-1}s^{-1}$)
l	constant (-)
Lb	bio-convection Lewis number (-)
Le	Lewis number (-)
m_w	surface mass flux
M	magnetic field parameter (-)
N	component of micro-rotation, i.e., angular velocity of micro-elements (s^{-1})
n	number of motile microorganisms (-)
n_1	number of motile microorganisms at lower plate (-)
n_2	number of motile microorganisms at upper plate (-)
n_w	wall motile microorganisms (-)
N_1	local velocity slip factor (sm^{-1}) -
Nb	Brownian motion parameter (-)
Nt	thermophoresis parameter (-)
$Nu_{\bar{r}}$	local Nusselt number (-)
p	fluid pressure (kg / ms^2)

$Pé$	bio-convection Péclet number (–)
Pr	Prandtl number (–)
q_w	surface heat flux (Wm^{-2})
q_n	surface micro-organism flux (–)
Q	heat source parameter (–)
$Q_{n\bar{r}}$	local microorganism number (–)
R	first-order chemical reaction parameter (–)
Re_x	local Reynolds number (–)
Sh_r	local Sherwood number (–)
t	time (s)
T	nanofluid temperature (K)
T_1	lower plate temperature (K)
T_2	upper plate temperature (K)
u	velocity component along the x – axis (ms^{-1})
v	velocity component along the y – axis (ms^{-1})
\tilde{v}	mean swimming velocity associated with micro-organisms
W_c	maximum cell swimming speed (ms^{-1})

Greek

α	thermal conductivity (m^2s^{-1})
β	squeeze number (–)
$\delta_\theta, \delta_\phi, \delta_\chi$	thermal, nano-particle concentration, and micro-organism wall constants (–)
γ_s	Eringen micropolar spin gradient viscosity ($kg\ ms^{-1}$)
$\chi(\eta)$	number density of motile microorganisms (–)
$\phi(\eta)$	nanoparticle volume fraction (–)
η	transverse similarity variable (–)
μ	dynamic viscosity of the fluid ($kgm^{-1}\ s^{-1}$)
ν	kinematic viscosity (m^2s^{-1})
$\theta(\eta)$	dimensionless temperature (–)
ρ	nanofluid density (kgm^{-3})
τ	ratio of the effective heat capacity of the nanoparticle material to the fluid heat capacity (Nm^{-2})
τ	shear stress (Nm^{-2})

ψ stream function ($m^2 s^{-1}$)

Subscripts

()' ordinary differentiation with respect to η .

1. INTRODUCTION

Magnetohydrodynamic (MHD) flows in parallel plate systems (ducts and channels) subject to various boundary conditions and have numerous applications in modern technologies. These include MHD pumps, MHD generators, crude oil purification, polymer processing, nuclear reactor heat transfer control, fusion energy, and electromagnetic flow meters. MHD involves the interaction of viscous electrically conducting fluids with an applied magnetic field [1]. A key area of modern MHD technology is magnetic lubrication. Lubricants with MHD properties provide enhanced flow control and improved thermal management capabilities. In this sense, they are smart lubricants as they can be modified to perform adaptively, especially in extreme conditions. Magnetic lubricants have been deployed in a variety of applications, including gears [2], sliding surfaces [3], and rolling bearings [4]. The working concepts of many mechanical devices are that of moving pistons, in which two plates show squeezing motion normal to their surfaces. This squeezing or clutching flow is exhibited in specific components of engines, hydraulic lifters, and electric motors. This practical importance has made squeezing flow between parallel plates an affluent area of fluid mechanics. Squeezing flow is a form of fluid motion that happens when a lubricant is intercalated between two tightly separated surfaces. The fluid flows in the small area between the surfaces due to the reduction in the gap between them, which characterizes this phenomenon. The Navier-Stokes equations explain the squeezing flow behavior for conventional Newtonian viscous liquids. However, the exact features of squeezing flow are determined by elements such as the fluid's composition, surface qualities, and external pressures applied. Squeezing flows have several fundamental aspects and applications, including lubrication, sealing, synovial (kneecap) tribology, polymer processing, and journal bearings. The study of squeezing flows uses mathematical modeling, computational simulations, and experimental approaches to obtain insight into fluid behavior in constrained places. Stefan [5] is credited with founding the field of squeezing flows, having developed the fundamental formulation of these flows under the lubrication assumption. Archibald [6] later obtained various squeeze films' load capacity and temporal relationships. Subsequent studies have explored various squeezing flows featuring multiple effects, including cross-diffusion, wall slip, and different squeezing rates. These studies have also deployed various numerical techniques to accommodate the nonlinear boundary value problems in squeezing flows. For example, Yinusa *et al.* [7] analyzed the combined effects of Soret and Dufour diffusion on

3-D rotating squeezing channel flow with wall slip conditions in an iterative approach. MHD squeezing flows have also received the attention of several researchers in recent years. Zueco and Bég [8] used PSPICE network electrothermal simulation software to study the influence of magnetic induction on the squeeze film flow of a magnetic lubricant between two parallel rotating disks. They noted that lower disk torque *remains negative* for all values of magnetic Reynolds number and rotational Reynolds number. In contrast, dimensionless axial and azimuthal magnetic fields are consistently elevated with increments in rotational Reynolds number. They further observed that the axial velocity is suppressed with counter-rotation of the disks and stronger squeezing. Bég et al. [9] employed the Adomian Decomposition Method (ADM) and Nakamura's finite difference method to investigate the effects of the squeeze Reynolds number, axial magnetic force strength parameter, and tangential magnetic force strength parameter on the flow characteristics of a Newtonian magnetic lubricant in a dual-disk squeeze regime. Shamshuddin *et al.* [10] deployed a variational parameter method (VPM) to simulate non-Fourier heat flux, viscous heating, and mass diffusion in Riga plate magnetic squeezing [9]. Prakash *et al.* [11] investigated electromagnetic time-dependent squeezing flow with variable thermophysical properties using MATLAB. They showed that axial velocity acceleration is achieved with higher electrical field strengths and negative squeeze numbers (plates approaching each other). In contrast, strong damping is produced with more significant magnetic field strengths. Balaji *et al.* [12] obtained numerical solutions for magnetized electrical ionic lubricant squeezing flow between rotating disks with zeta potential effects. They noted that pressure is boosted close to the disk walls with stronger magnetic and electrical fields and squeezing parameters, whereas with greater wall suction, a strong damping effect is produced in both radial and transverse velocity fields.

The above studies were confined to Newtonian lubricants. However, Many studies have shown that rheological characteristics are common in effective squeeze lubrication, including lithium complex grease [13], magnetic liquids deployed in journal bearings [14, 15], etc. Magnetic non-Newtonian squeezing films have been studied by for example Mekheimer *et al.* [16] (who used the Casson viscoplastic model), Wang *et al.* [17] (who used a Bingham viscoplastic magneto-rheological model), Hayat *et al.* [18] (who implemented a Reiner-Rivlin second grade viscoelastic model) and Muhammed *et al.* [19] (who investigated magnetic Carreau squeezing flow in a micro-cantilever sensor). These studies confirmed the beneficial effect of magnetic field in controlling squeeze film performance and load capacity.

Lubrication engineering often features fluids with microstructure which comprise of suspensions in viscous liquids. This results in a deviation from Newtonian behavior and conventional non-Newtonian models for their accurate simulation. Various such models exist, including polar Stokesian fluids and the more general Eringen micropolar model [20]. These models are more comprehensive than the more

common non-Newtonian models deployed for viscoelastic, viscoplastic, and other non-Newtonian lubricants, such as the Casson, Bingham plastic, and Maxwell viscoelastic models. From a physical perspective, micropolar fluids may be composed of inflexible, randomly arranged particles suspended in a viscous medium, with no consideration given to the fluid particles' deformation. Unlike classical fluid mechanics, which posits that fluids are continuous with no internal structure, micropolar fluid models account for non-Newtonian fluids' underlying microscale characteristics and structure. The micropolar fluid model is distinguished by an additional set of equations that simulate micro-rotation (spin of micro-elements) and micro-inertia phenomena. Micropolar fluid theory provides a robust framework that enables the extraction of the traditional Navier-Stokes equations for Newtonian behavior, as a special case when micro-rotation (angular momentum) effects are negated. Micropolar fluids have proved very successful in modeling a range of complex industrial and biological fluids, including polymer suspensions, slurries, blood, liquid crystals, and sophisticated lubricants. While the classical Navier-Stokes viscous model is frequently sufficient for many engineering applications, micropolar fluid models provide a more refined approach when microstructure effects are prominent. In tribology, the micropolar model has been used by Dhawan *et al.* [21] (for noncircular hybrid journal bearings) and Nair *et al.* [22] (for elastohydrodynamic elliptical journal lubrication). Magnetized micropolar squeezing flows have also received some attention in recent years, mainly due to applications in bright lubrication in biomechanics (e.g., prosthetics) and aerospace technologies (e.g. spacecraft landing gear systems). Hayat *et al.* [23] used the homotopy analysis method (HAM) to compute the magnetic micropolar squeeze film between parallel approaching plates. They showed that squeezing parameter and magnetic field intensity strongly influence skin friction and wall couple stress (micro-rotation gradient). Bég *et al.* [24] deployed numerical shooting methods and homotopy analysis methods to simulate the unsteady magnetohydrodynamic micropolar squeeze film in a kneecap geometry containing a rigid porous medium. They computed the impact of Hartmann magnetic number, micropolar spin gradient viscosity parameter, and unsteadiness parameter on linear and angular velocity (micro-rotation). They showed that a stronger magnetic field suppresses linear and angular velocity and produces a greater load capacity at specific permeability and porosity values. Another significant development in recent years has been *nanofluid* technology. Nanofluids are complex colloidal suspensions that comprise a base fluid, usually a liquid like water or oil, and nanoparticles. Nanofluids were pioneered by Choi [25] originally for automotive applications. The nanoparticles in nanofluids are often metallic or ceramic and range in size from 1 to 100 nanometers. Nanofluids offer superior thermal, rheological, and wettability properties that improve the performance of several applications, including heat transfer, lubrication, medication administration, and increased oil recovery. Nanofluids outperform microfluids in terms of stability and heat conduction. Due to the

importance of these materials in various thermal engineering applications and industrial settings, the synthesis of nanofluids has garnered significant interest from scientists and engineers. Many contributions are made to this topic, particularly in the current century, since nanofluids have a diverse range of uses in various technological and industrial processes, including solar collectors, cooling of electronic components, anti-bacterial biotechnology, heat exchangers, generators, nuclear reactors, propellants, etc. Buongiorno developed a robust two-component nanofluid model that includes heat and mass (nanoparticle) diffusion and emphasizes the dominant role of thermophoresis and Brownian motion. Tribological studies using nanofluids have demonstrated their effectiveness in reducing friction and wear in lubrication, offering a promising avenue for designing energy-efficient systems. Nanofluids have been employed in large machinery squeeze film lubricants [26], manufacturing [27], and other areas [28]. Mathematical models of squeezing flows of nanofluids have also garnered some attention. Rashid *et al.* [29] used a homotopy analysis method to simulate the influence of nanoparticle shape factor in gold-water nanofluid squeezing nanofluid flow and heat transfer between parallel plates. They considered column, sphere, hexahedron, tetrahedron, and lamina geometries and noted that the Nusselt number is the maximum for lamina and spherical-shaped nanoparticles. Magnetohydrodynamic nanofluid squeeze films have also been examined extensively. Ahmad *et al.* [30] studied the transient hydromagnetic dissipative squeezing flow and heat transfer in a Tiwari-Das nanofluid between rotating parallel plates with entropy generation. They considered the relative performance of five different metallic/metallic oxide nanoparticles (titania, alumina, copper oxide, copper, and silver) and water-based fluid and solved the dimensionless boundary problem with the Mathematica ND Solve routine. They showed that the axial flow is decelerated with increasing squeezing variables, whereas temperature is elevated with magnetic parameters, Eckert numbers, nanoparticle volume fractions, and squeezing variables. They also observed that entropy generation is elevated with larger values of Prandtl and Eckert numbers. Hayat *et al.* [31] obtained analytical power series solutions for unsteady magnetic squeezing couple stress Buongiorno nanofluid flow between approaching parallel plates. They noted that an increment in squeezing parameter suppresses temperature and nanoparticle concentration, whereas Brownian motion enhances them. The reverse influence is however computed on temperature as compared with concentration (volume fraction) with increasing thermophoresis parameter. Bég *et al.* [32] computed the unsteady squeezing flow of a magnetic Buongiorno nanofluid between squeezing surfaces using a B-spline collocation numerical method to simulate prosthetic smart tribology. They computed the effects of nanoparticle volume fraction, squeeze number, Hartmann magnetic body force number, disk surface transpiration parameter, Brownian motion parameter, thermophoretic parameter, Prandtl number, and Lewis number on transport characteristics. Further studies include Ramesh *et al.* [33] (who considered

magnetic squeezing of Casson-micropolar nanofluid with transpiration and slip effects), Umavathi *et al.* [34] (who considered mixed boundary Robin condition effects on time-dependent squeezing flow of magnetized Buongiorno nanofluids), Khashiie *et al.* [35] (who simulated magnetized squeezing flow of Cu-Al₂O₃/water hybrid nanofluid) and Usha and Shankar [36] (who included chemical reaction and Ohmic magnetic dissipation effects on unsteady squeezing flow).

Bioconvection is a remarkable phenomenon exhibited in microorganism self-organization and dynamic behavior in response to environmental signals (taxes). Bioconvection serves as a paradigmatic example wherein large-scale phenomena emerge from the microscopic actions of cells within moderately diluted systems. It is observed in various situations, including aquatic bodies, where microorganisms such as algae, bacteria, and other planktonic organisms demonstrate coordinated motion. Bioconvection finds applications in diverse domains such as pharmaceuticals, the synthesis of biological polymers, eco-friendly solutions, sustainable fuel cell technologies, microbial-enhanced oil recovery, biosensors, biotechnology, etc. Vincent and Vincent examined a floating algae solution [37] to experimentally study the bioconvection process. Plesset and Winet [38] developed the first theoretical model of bioconvection, which applies to a wide range of motile microorganisms, including gyrotactic (torque-driven), chemo-tactic (chemically driven), oxytactic (oxygen-driven), etc. In recent years, bioconvection has also been considered for biofuel and bio-lubricant applications [39]. In the latter, vegetable oils, plant polymeric carbohydrates and wax esters are often used, and microorganisms can be embedded within these fluent materials. The transesterification of vegetable oils generates fatty acid alkyl esters of varying alcohol chain lengths [40]. Chemical reactions can be catalyzed successfully by mineral acids and bases, and the generated fatty acid alkyl esters can be deployed as biodiesel fuel and bio-tribological materials [41, 42].

The idea of *bioconvection nanofluids* combines the contributions of self-propelled microorganisms and nanoparticles to achieve improved thermal performance in biofuels and bio-lubricants. The collective interplay of denser self-propelled microorganisms and smaller nanoparticles with buoyancy forces can be manipulated to achieve density stratification and significant modifications in viscosity and thermal conductivity, enhancing the efficiency of working fluids. Koriko *et al.* [43] have studied the effects of magnetic field on gyrotactic bioconvection in nanofluids. Squeezing flows featuring bioconvection phenomena have been reported by Acharya *et al.* [44] (with higher-order chemical reactions and hydrodynamic wall slip effects). Shamshuddin *et al.* [45] considered homogenous chemical reaction effects in transient squeezing flow of magnetized bioconvection lubricants with MATLAB bvp4c quadrature and a successive Taylor series linearization method (STSLM) utilizing Chebyshev interpolating polynomials and Gauss-Lobatto collocation. They showed that the magnetic field damps the axial flow whereas bioconvection Peclet number induces

acceleration and strongly modifies temperature and micro-organism density number. Zeeshan *et al.* [46] used a differential transform method (DTM) combined with Padé approximants to investigate the bioconvective Buongiorno nanofluid squeezing flow between rotating and approaching circular plates with thermal radiative heat transfer. They showed that both axial and tangential flow are damped with greater squeezing Reynolds number, whereas greater temperatures are produced with more vigorous radiation parameters. Srinivasacharya and Sreenath [47] used a Chebyshev collocation method to compute the bioconvective micropolar squeezing flow between stretching parallel plates. They showed that a more significant squeezing parameter enhances flow acceleration and boosts temperature but suppresses local Nusselt and Sherwood numbers. They further noted that motile microorganism density is reduced with more significant squeezing parameter, bioconvection Lewis number, bioconvection Peclet number, and bioconvection Schmidt number. Recently, Yasmin *et al.* [48] studied water-based hybrid nanofluid with nanoparticles and gyrotactic microorganisms over a stretching surface with convective conditions. They found that the microorganisms' distribution decreased by the bioconvection Peclet and Lewis numbers. The density number has been decreased by the bioconvection Peclet and Lewis numbers.

In the present work, we generalized previous studies to consider *micropolar nanofluid MHD squeezing with Stefan blowing, chemical reaction, and heat source effects*. Chemical reaction effects are important in lubrication applications where oxidation is associated with the chemical degradation of lubricants and debris generated by wear, which acts as a catalyst to induce degradation, including boundary damage, contaminants, swarfing, corrosion, etc.[48-50]. The state in which a species diffuses along an interface is known as Stefan blowing [51]. Stefan blowing effect is the term for the bulk motion of fluids caused by species diffusion, as elaborated by Fang and Jing [52]. The Stefan blowing influences fluid bulk motion and species transfer depending on the flow field. For this reason, modeling the flow requires a link between momentum and concentration. Hamid *et al.* [53] considered many applications of Stefan blowing, such as evaporation in petrochemical processes and drying processes in which a mass flow exists from the surface to the surrounding area. It can also arise in lubrication systems, including squeezing regimes. It should be mentioned that Stefan blowing differs from conventional blowing (due to transpiration or mass injection). Stefan blowing is associated with an impermeable surface; injection or transpiration-related blowing requires a porous surface.

Unlike previous works that have considered individual effects such as MHD squeezing flows, bioconvection, Stefan blowing, or chemical reactions in isolation, the present study is the first to integrate these phenomena into a single unified framework for an unsteady magnetohydrodynamic squeezing flow of a micropolar Buongiorno nanofluid between parallel plates. Specifically, the model simultaneously incorporates gyrotactic microorganism bioconvection, Stefan blowing, first-order

homogeneous chemical reaction, and internal heat generation effects, which have not been previously analyzed in combination within the context of micropolar nanofluids. Additionally, this work adopts Eringen's micropolar fluid theory to capture micro-rotation and vortex viscosity effects, offering a more realistic representation of microstructural behavior in non-Newtonian nanofluids compared to traditional Newtonian or generalized non-Newtonian models. The Buongiorno two-component model further distinguishes this study by accurately capturing nanoparticle transport via Brownian motion and thermophoresis mechanisms. Through detailed parametric analysis and validation against limiting cases from prior studies, the proposed model provides novel insights into the interplay of these complex effects, filling a significant gap in the literature and advancing the understanding of smart bio-nano-lubrication and thermal management systems.

2.MATHEMATICAL MODEL

Figure 1 depicts the physical model of an unsteady squeezing flow of a magnetic bio-nano-convective micropolar fluid between two parallel plates. The upper plate moves towards or away from the stationary lower plate, simulating squeezing or separation, with Stefan blowing applied at the upper surface to enhance mass transfer. A perpendicular magnetic field influences the micropolar nanofluid, which contains gyrotactic microorganisms inducing bioconvection. The system also incorporates internal heat generation and first-order chemical reactions. Key transport variables—velocity, temperature, nanoparticle concentration, and microorganism density—vary across the gap, demonstrating the combined effects of MHD, bioconvection, and micro-rotation in a smart lubrication context. The plates are separated by the distance $h(t) = \sqrt{\frac{v}{b}(1 - at)}$. A varying magnetic field of strength $B * (t) = B_0(1 - at)^{-1/2}$ is applied normally to the lower and upper stationary plates. First order chemical reaction, and heat source are also considered. Physical properties are assumed to be constant. Stefan blowing is considered at the upper plate. The physical regime is illustrated in **Figure 1**.

1.

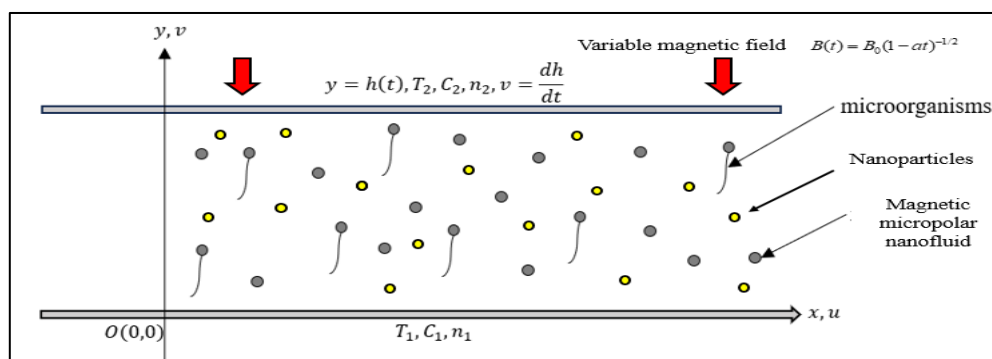


Figure 1: Squeezing film regime of magnetic bio-nano-convective micropolar fluid.

Nanoparticles and gyrotactic microorganisms do not interact. The upper plate $y = h(t)$ moves towards or away from the stationary lower plate with velocity $\frac{dh}{dt}$. In the case of $a > 0$, the two plates being squeezed until they touch $t = 1/a$, For the case $a < 0$, the two plates are separated. Hall current and magnetic induction are neglected, and the inner plate surfaces are electrically insulated. With the assumptions mentioned above, the conservation equations, i.e., *mass, momentum, energy, nanoparticles volume fraction, and density of motile microorganisms*, may be stated by extending the model of Raees *et al.* [54] to consider non-Newtonian micropolar chemical reaction and heat source effects as follows:

Continuity equation (mass conservation), ensuring the incompressibility of the micropolar nanofluid:

$$\frac{\partial u}{\partial x} + \frac{\partial v}{\partial y} = 0, \quad (1)$$

Momentum equation in the X-direction, including effects from pressure gradients, viscous forces, magnetic body force, and the micropolar coupling:

$$u_t + uu_x + vv_y = -\frac{1}{\rho} p_x + \left(\frac{\mu + k_1}{\rho} \right) (u_{xx} + u_{yy}) + \frac{k_1}{\rho} N_y - \frac{\sigma B^2(t)}{\rho} u, \quad (2)$$

Momentum equation in the Y-direction for a micropolar fluid, specifically within the context of Eringen's micropolar fluid theory, including convective terms, pressure gradient force, coupling term between the velocity field and the microrotation field N :

$$v_t + uv_x + vv_y = -\frac{1}{\rho} p_y + \left(\frac{\mu + k_1}{\rho} \right) (v_{xx} + v_{yy}) - \frac{k_1}{\rho} N_x, \quad (3)$$

Angular momentum (micro-rotation) equation, including the diffusion of angular momentum, vortex viscosity, and micro-inertia density effects:

$$N_t + uN_x + vN_y = -\left(\frac{k_1}{\rho j(t)} \right) (2N + u_y - v_x) + \gamma_s^* (N_{xx} + N_{yy}) \frac{1}{\rho j}, \quad (4)$$

Energy equation, accounting for heat conduction, convective heat transfer, internal heat generation (heat source parameter Q), and the contributions from Brownian motion (Nb) **and** thermophoresis (Nt) effects:

$$T_t + uT_x + vT_y = \alpha (T_{xx} + T_{yy}) + \tau D_B C_y T_y + \frac{D_T}{T_0} (T_y)^2 + \frac{Q_s(t)}{\rho c_p} (T - T_0), \quad (5)$$

Nanoparticle concentration (NPVF) equation, which includes terms for Brownian diffusion, thermophoretic diffusion, and first-order chemical reaction (parameter R):

$$C_t + uC_x + vC_y = D_B C_{yy} + \frac{D_T}{T_0} T_{yy} - c(t)(C - C_0), \quad (6)$$

Density of motile microorganisms, capturing bioconvection effects influenced by chemotaxis and swimming behavior of gyrotactic microorganisms:

$$n_t + un_x + vn_y + \frac{\partial}{\partial y}(n\tilde{v}) = D_n n_{yy}. \quad (7)$$

The relevant boundary conditions imposed at the lower and upper plates, following Fang and Jing [52], are:

$$u = 0, v = \frac{-D_B}{(1-C_1)} \frac{\partial C}{\partial y}, N = -l \frac{\partial u}{\partial y}, T = T_1, C = C_1, n = n_1 \quad \text{at } y = 0,$$

$$u = 0, v = \frac{dh}{dt}, N = 0, T = T_2, C = C_2, n = n_2 \quad \text{at } y = h(t). \quad (8)$$

In Eqns. (1)-(8) the following notation applies: (u, v): velocity components along axes, t (time), T, C, N and n (temperature, nanoparticle volume fraction, angular velocity of micro-elements and microorganisms), B * (magnetic field strength), $C(t)$: reaction constant, $Q(t)$: heat source, γ_s (Eringen micropolar spin gradient viscosity), j (micro-inertia density), k_1 (micropolar vortex viscosity coefficient), (T_1, T_2) (temperature at lower and upper plates), (C_1, C_2) (NPVF at lower and upper plates), (N_1, N_2) (density of microorganism at lower and upper plates), ν (kinematic viscosity), p (fluid pressure), ρ (density), α (thermal diffusivity), τ (ratio of heat capacity of nanoparticle to fluid), D_B (Brownian diffusion coefficient), D_T (thermophoretic diffusion coefficient), and D_n (microorganism diffusivity coefficient), $\tilde{v} \left(= \frac{\tilde{b} W_c}{\Delta C} \frac{\partial C}{\partial y} \right)$ (mean swimming velocity associated with microorganisms), \tilde{b} (chemotaxis constant), W_c (maximum cell swimming speed). According to Eringen [20], l is the non-dimensional particle concentration difference, which specifies the degree of rotation of microelements close to the channel walls and diverges in the range of $0 \leq l \leq 1$. Here $l = 0$ implies that micropolar fluid has substantial particle concentration; around the wall, the microelements are very tightly packed and incapable of spinning or rotating, whilst $l = 0.5$ indicates that the micropolar fluid has reduced particle concentration; antisymmetric portion of the stress tensor is about to vanish, and $l = 1$ represents turbulent flow (which is not considered here).

3.SIMILARITY EQUATIONS

Following Raees *et al.* [54], we deploy the following coordinate transformations:

$$\begin{aligned}
 u &= \frac{bx}{(1-at)} f'(\eta), \quad v = -\frac{\sqrt{bv}}{\sqrt{1-at}} f(\eta), \quad N = \sqrt{\frac{b^3}{(1-at)^3 v}} xh(\eta), \quad \eta = y\sqrt{\frac{b}{(1-at)v}}, \\
 Q &= \frac{Q_s(1-at)}{\rho C_p b}, \quad R = \frac{c(t)(1-at)}{b}, \quad T = T_0 + \Delta T \theta(\eta), \\
 C &= C_\infty + \Delta C \phi(\eta), \quad n = \Delta n \chi(\eta), \quad j(t) = j_0(1-at), \quad \gamma_s^* = \left(\mu + \frac{k_1}{2} \right) j.
 \end{aligned} \tag{9}$$

Here $f(\eta)$ is the dimensionless stream function, $h(\eta)$ is dimensionless angular velocity (micro-rotation), $\theta(\eta)$ dimensionless temperature, NPVF, the number density of motile microorganisms, and all other parameters are defined in the notation section. Using (9), Eqns. (1)-(7) are transformed into an 11th order system of coupled nonlinear ordinary differential equations:

$$3\beta f'' + \beta \eta f'' + f' f'' - ff''' - (1+K)f'''' - K h'' + M f'' = 0, \tag{10}$$

$$(1+K/2)h'' + \beta(3h + \eta h') + (f'h - fh') + B(2h + f'') = 0, \tag{11}$$

$$\theta'' + \text{Pr}[Q\theta - \beta\eta\theta' + f\theta'] + Nb\phi'\theta' + Nt(\theta')^2 = 0, \tag{12}$$

$$\phi'' + \frac{Nt}{Nb}\theta'' - \text{Pr}Le[R\phi + \beta\eta\phi' - f\phi'] = 0, \tag{13}$$

$$\chi'' + \frac{1}{Sc}(-\beta\eta\chi' + f\chi') - Pe[\chi\phi'' + \phi'\chi'] = 0. \tag{14}$$

The boundary conditions in Eq. (8) become:

$$\begin{aligned}
 f'(0) = 0, \quad f(0) = \frac{S}{Le \text{Pr}} \phi'(0), \quad \theta(0) = \phi(0) = \chi(0) = 1, \quad h(0) = -lf''(0). \\
 f'(1) = 0, \quad f(1) = \beta, \quad \theta(1) = \delta_\theta, \quad \phi(1) = \delta_\phi, \quad \chi(1) = \delta_\chi, \quad h(1) = 0.
 \end{aligned} \tag{15}$$

The multi-physical dimensionless parameters featured in Eqs. (10)-(15) are defined as follows:

$$\begin{aligned}
 \beta &= \frac{a}{2b}, \quad (\text{squeeze number}), \quad M = \frac{\sigma B^2(1-at)}{\rho b} \quad (\text{magnetic field parameter}), \quad \text{Pr} = \frac{\nu}{\alpha} \quad (\text{Prandtl number}), \\
 K &= \frac{k_1}{\mu} \quad (\text{Eringen microrotation vortex viscosity parameter}), \quad Nb = \frac{\tau D_B \Delta C}{\alpha} \quad (\text{Brownian motion parameter}), \\
 Nt &= \frac{\tau D_T \Delta T}{T_0 \alpha} \quad (\text{thermophoresis parameter}), \quad Sc = \nu/D_n, \quad Le = \frac{\alpha}{D_B} \quad (\text{Lewis number}), \quad Lb = \frac{\alpha}{D_n}
 \end{aligned}$$

(bioconvection Lewis number), $Pe = \frac{\tilde{b}W_c}{D_n}$ (bioconvection Péclet number), $s = \frac{\Delta C}{1-C_1}$ (Stefan

suction/blowing parameter), $Q = \frac{Q_0}{\rho C_p b}$ (heat source parameter), $R = \frac{c(t)(1-at)}{b}$ (first order chemical

reaction parameter), $B = \frac{k_1}{\rho j_0 b}$ (microinertia density parameter).

$\delta_\theta = \frac{T_1 - T_0}{T_2 - T_0}$, $\delta_\phi = \frac{C_1 - C_0}{C_2 - C_0}$, $\delta_\chi = \frac{n_1 - n_0}{n_2 - n_0}$ are respectively, thermal, nanoparticle, and micro-organism

boundary (wall) parameters. Note that $\beta > 0$ corresponds to the accelerating plates moving apart and the decelerating plates moving together (the so-called “squeezing flow”), respectively. Also note that for $s > 0$, mass is being expelled from the surface (e.g., micropolar nanofluid being released from a plate surface) whilst for $s < 0$, mass is being absorbed into the surface (e.g., micropolar nanofluid suction).

The presented model has several limitations based on simplifying assumptions. It neglects magnetic induction and Hall current effects by assuming a low magnetic Reynolds number and electrically insulated plates, which may not apply to highly conductive fluids or strong magnetic fields. The Buongiorno nanofluid model assumes no slip between nanoparticles and fluid and ignores particle shape, agglomeration, and interactions with microorganisms. Constant physical properties are considered, excluding temperature-dependent variations in viscosity and conductivity. The model also simplifies the bioconvection process by assuming non-interacting microorganisms and focuses on a two-dimensional parallel plate geometry, which does not capture three-dimensional or complex boundary effects. These limitations suggest directions for future improvements to enhance model realism and applicability.

4. PHYSICAL QUANTITIES

The physical quantities relevant to engineering tribology are the velocity gradients, temperature, nanoparticle concentration, and motile micro-organism density number, i.e., *local skin friction factor*, *Nusselt number*, *nanoparticle Sherwood number*, and the *wall motile microorganism gradient*. They are defined as:

$$C_f = \frac{\tau_w}{\rho U_w^2}, \quad Nu_x = \frac{x q_w}{k \Delta T}, \quad Sh_x = \frac{x j_w}{D_B \Delta C}, \quad (16)$$

$$Nn_x = \frac{x P_w}{D_n \Delta n},$$

Here τ_w, q_w, j_w and, p_w the shear stress, heat flux, surface nanoparticle flux, and surface motile microorganism flux are represented, respectively. They may be defined as:

$$\begin{aligned} \tau_w &= (\mu + k_1) \left[\frac{\partial u}{\partial y} + k_1 N \right]_{y=0}, \quad q_w = -k \left(\frac{\partial T}{\partial y} \right)_{y=0}, \\ j_w &= -D_B \left(\frac{\partial C}{\partial y} \right)_{y=0}, \quad p_w = -D_n \left(\frac{\partial n}{\partial y} \right)_{y=0}. \end{aligned} \quad (17)$$

Via introducing the transformations in Eq. (9), we obtain the desired expressions for *local skin friction*, *local Nusselt number*, *local nanoparticle Sherwood number*, and *local motile micro-organism density gradient*, as:

$$\begin{aligned} \text{Re}_x^{1/2} C_f &= [1 + K(1-l)] f''(0), \quad \text{Nu}_x \text{Re}_x^{-1/2} = -\theta'(0), \quad \text{Sh}_x \text{Re}_x^{-1/2} = -\phi'(0), \\ \text{Nn}_x \text{Re}_x^{-1/2} &= -\chi'(0). \end{aligned} \quad (18)$$

Here $\text{Re}_x = \frac{U_w x}{\nu}$ is the *local Reynolds number* in which $U_w = \frac{bx}{(1-at)}$.

5. NUMERICAL SOLUTION OF TRIBOLOGICAL BOUNDARY VALUE PROBLEM

Equations (10)-(14), along with the boundary conditions in Eq. (15), have been numerically solved using Maple 24.0. The software employs the 4th/5th order Runge-Kutta-Fehlberg (RKF) method for solving boundary value problems, a technique known for its accuracy and robustness. To further validate the Maple 24 numerical algorithm, the method was applied to a constant surface temperature case previously studied by other authors, and their results were accurately reproduced. To ensure convergence for all governing parameters in this study, the unity coefficient in the relevant term was replaced with (101, 100), and the continuation lambda was implemented in the “dsolve” command. Without this modification, Maple 24 returned results that failed to achieve correct asymptotic behavior, instead showing intersections with the *h*-axis at steep angles. The appropriate modifications achieve the required convergence in Maple 24. The stepping formulae although designed for nonlinear problems, are even more efficient for any order of linear differential equation and are summarized below :

$$k_0 = f(x_i, y_i), \quad (19)$$

$$k_1 = f\left(x_i + \frac{1}{4}h, y_i + \frac{1}{4}hk_0\right), \quad (20)$$

$$k_2 = f\left(x_i + \frac{3}{8}h, y_i + \left(\frac{3}{32}k_0 + \frac{9}{32}k_1\right)h\right), \quad (21)$$

$$k_3 = f\left(x_i + \frac{12}{13}h, y_i + \left(\frac{1932}{2197}k_0 - \frac{7200}{2197}k_1 + \frac{7296}{2197}k_2\right)h\right), \quad (22)$$

$$k_4 = f\left(x_i + h, y_i + \left(\frac{439}{216}k_0 - 8k_1 + \frac{3860}{513}k_2 - \frac{845}{4104}k_3\right)h\right), \quad (23)$$

$$k_5 = f\left(x_i + \frac{1}{2}h, y_i + \left(-\frac{8}{27}k_0 + 2k_1 - \frac{3544}{2565}k_2 + \frac{1859}{4101}k_3 - \frac{11}{40}k_4\right)h\right), \quad (24)$$

$$y_{i+1} = y_i + \left(\frac{25}{216}k_0 + \frac{1408}{2565}k_2 + \frac{2197}{4101}k_3 - \frac{1}{5}k_4\right)h, \quad (25)$$

$$z_{i+1} = z_i + \left(\frac{16}{135}k_0 + \frac{6656}{12825}k_2 + \frac{28561}{56430}k_3 - \frac{9}{50}k_4 + \frac{2}{55}k_5\right)h. \quad (26)$$

Here y denotes fourth order Runge-Kutta-Fehlberg phase and z is the fifth order Runge-Kutta-Fehlberg phase.

An estimate of the error is achieved by subtracting the two values obtained. If the error exceeds a specified threshold, the results can be re-calculated using a smaller step size. The approach to estimating the new step size is shown below:

$$h_{new} = h_{old} \left(\frac{\varepsilon h_{old}}{2|z_{i+1} - y_{i+1}|} \right)^{1/4}. \quad (27)$$

The 4th-5th order Runge-Kutta-Fehlberg (RKF45) method offers several advantages over other numerical techniques, particularly for solving complex, nonlinear boundary value problems like those in this study. One of its key strengths is the adaptive step size control, which adjusts the step size dynamically based on local error estimation, ensuring high accuracy while optimizing computational efficiency. Unlike fixed-step methods such as the classical fourth-order Runge-Kutta, RKF45 reduces computational time by taking larger steps in regions of slow variation and smaller steps where greater precision is needed. It is particularly effective for nonlinear and stiff systems, providing better stability than lower-order methods like Euler's approach. Furthermore, RKF45 does not require the computation of derivatives of the governing equations, making its implementation simpler than implicit schemes such as backward differentiation formulas. When combined with the shooting

method, RKF45 efficiently transforms boundary value problems into initial value problems, allowing for accurate and robust solutions. Its compatibility with symbolic computational tools, such as Maple 24 used in this study, makes RKF45 an excellent choice for handling complex multiphysics simulations with high precision and reliability.

6. VALIDATION WITH PREVIOUS STUDIES

In the case of regular Newtonian viscous fluid without nanoparticles ($Nb \rightarrow 0, Nt \rightarrow 0$) and in the absence of micropolar effects (for which Eq. (6) and associated micro-rotation boundary conditions vanish), the present mathematical model retracts exactly to that studied by Zhao *et al.* [55] when $s = 0$. Therefore, Maple 24 numerical results have been validated by comparing them with the solutions obtained by Zhao *et al.* [55]. **Table 1** shows the comparison values of the local Sherwood number $Sh_x Re_x^{-1/2}$ and **Table 2** documents the comparison for local Nusselt number $Nu_x Re_x^{-1/2}$. In both cases, we consider different values of the thermal wall parameter δ_θ and magnetic parameter, M .

Table 1. Comparison of values of the local Sherwood number $Sh_x Re_x^{-1/2}$ for different values of δ_θ and M with Zhao *et al.* [55].

δ_θ	$M=0$		$M=50$		$M=100$	
	Zhao <i>et al.</i> [55]	Maple 24	Zhao <i>et al.</i> [55]	Maple 24	Zhao <i>et al.</i> [55]	Maple 24
0	0.62504	0.62503	0.68927	0.68927	0.75182	0.75181
0.2	0.39363	0.39362	0.44398	0.44397	0.49285	0.49284
0.4	0.16221	0.16221	0.19868	0.19868	0.23388	0.23388
0.6	-0.06921	-0.06921	-0.04661	-0.04661	-0.02509	-0.02509
0.8	-0.30062	-0.30062	-0.29191	-0.29191	-0.28406	-0.28406
1	-0.53204	-0.53203	-0.53721	-0.53720	-0.54303	-0.54303

Table 2. Comparison of values of the local Nusselt number $Nu_x Re_x^{-1/2}$ for different values of δ_θ and M . with Zhao *et al.* [55]

δ_θ	$M=0$		$M=50$		$M=100$	
	Zhao <i>et al.</i> [55]	Maple 24	Zhao <i>et al.</i> [55]	Maple 24	Zhao <i>et al.</i> [55]	Maple 24
0	1.28437	1.28427	1.33808	1.33798	1.39126	1.39116
0.2	1.11792	1.11783	1.16167	1.16158	1.20508	1.20499
0.4	0.95147	0.95139	0.98525	0.98517	1.01890	1.01882
0.6	0.78501	0.78495	0.80883	0.80877	0.83271	0.83265
0.8	0.61856	0.61851	0.63242	0.63237	0.64653	0.64648
1	0.45210	0.45207	0.45600	0.45597	0.46035	0.46031

7. RESULTS AND DISCUSSION

In all the plots, physically relevant data is utilized based on industrial lubrication systems [2-4] and previous numerical studies [52-55].

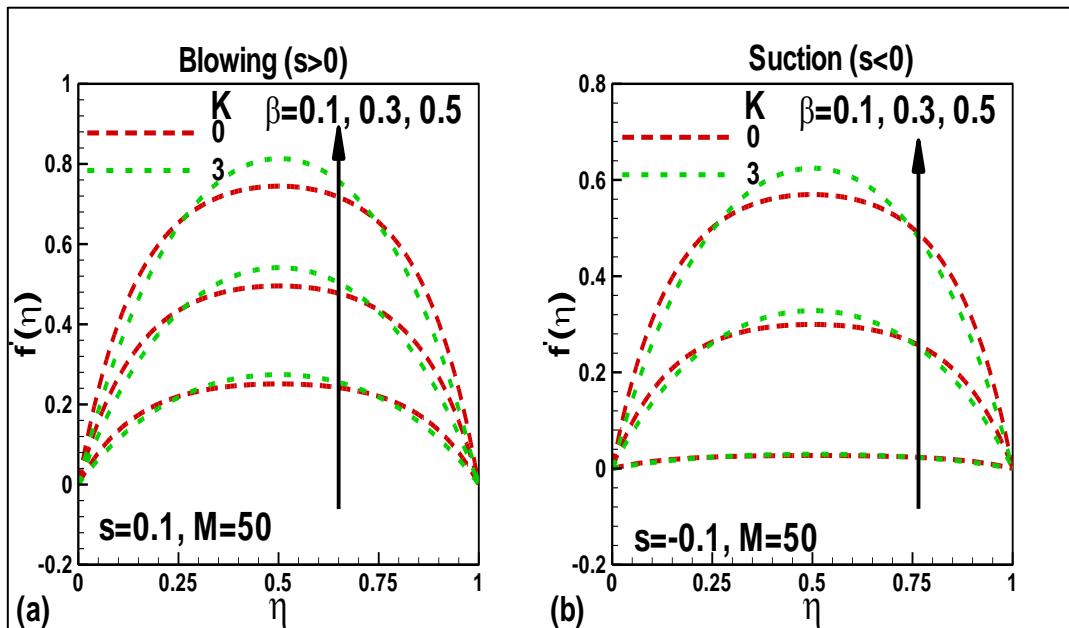


Figure 2: Effects of microrotation parameter (K) and squeeze number (β) on dimensionless linear velocity for a) blowing and b) suction.

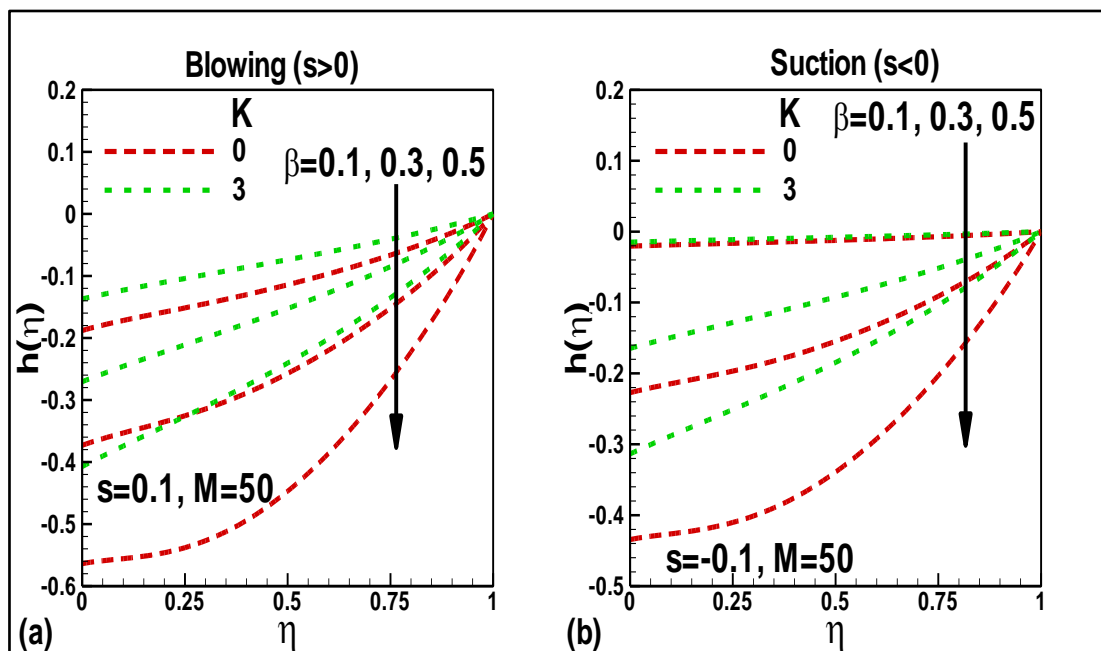


Figure 3: Effects of microrotation parameter (K) and squeeze number (β) on dimensionless angular velocity for a) blowing and b) suction.

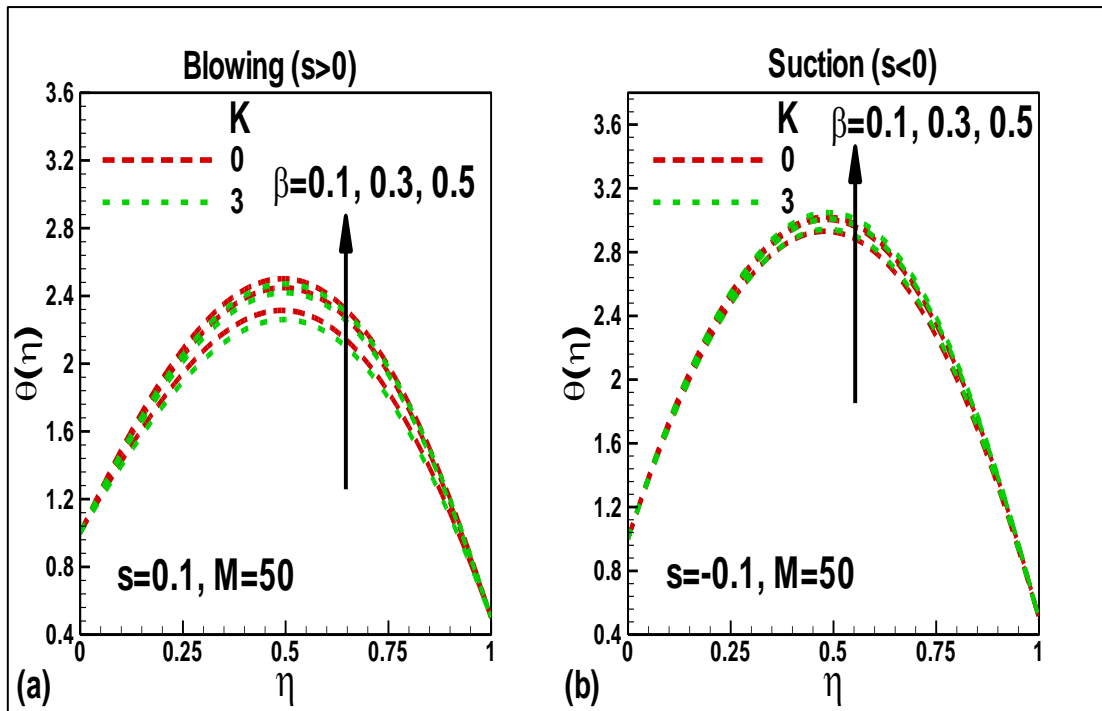


Figure 4: Effects of microrotation parameter (K) and squeeze number (β) on dimensionless temperature for a) blowing and b) suction.

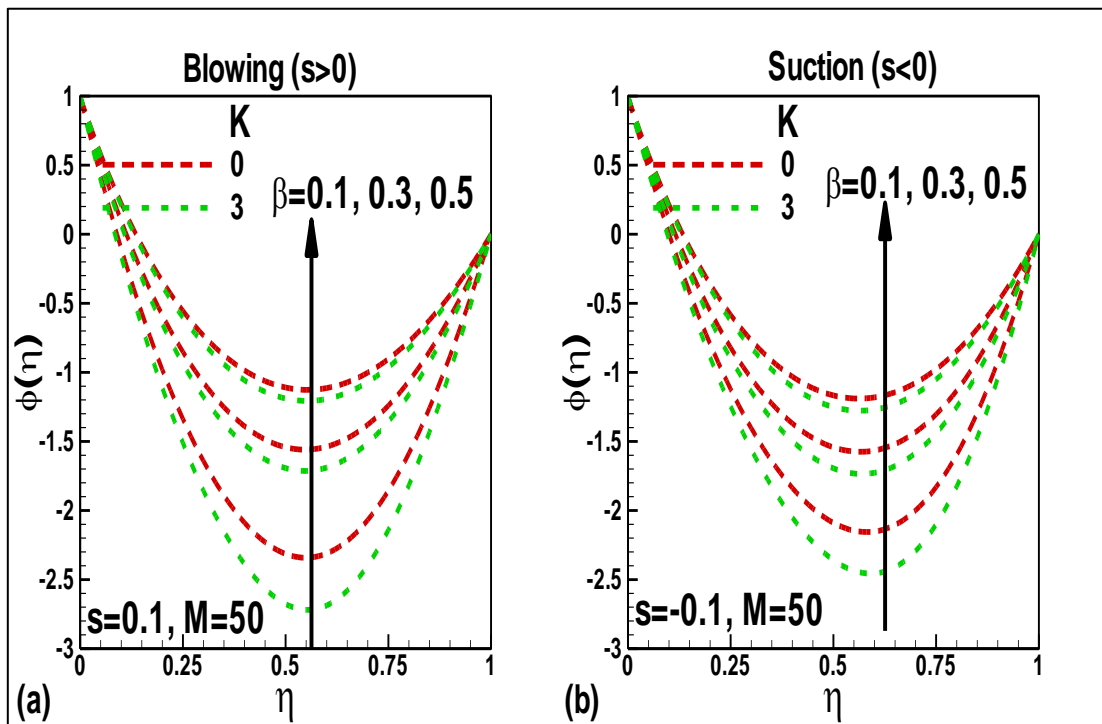


Figure 5: Effects of microrotation parameter (K) and squeeze number (β) on dimensionless nanoparticle concentration (volume fraction) for a) blowing and b) suction.

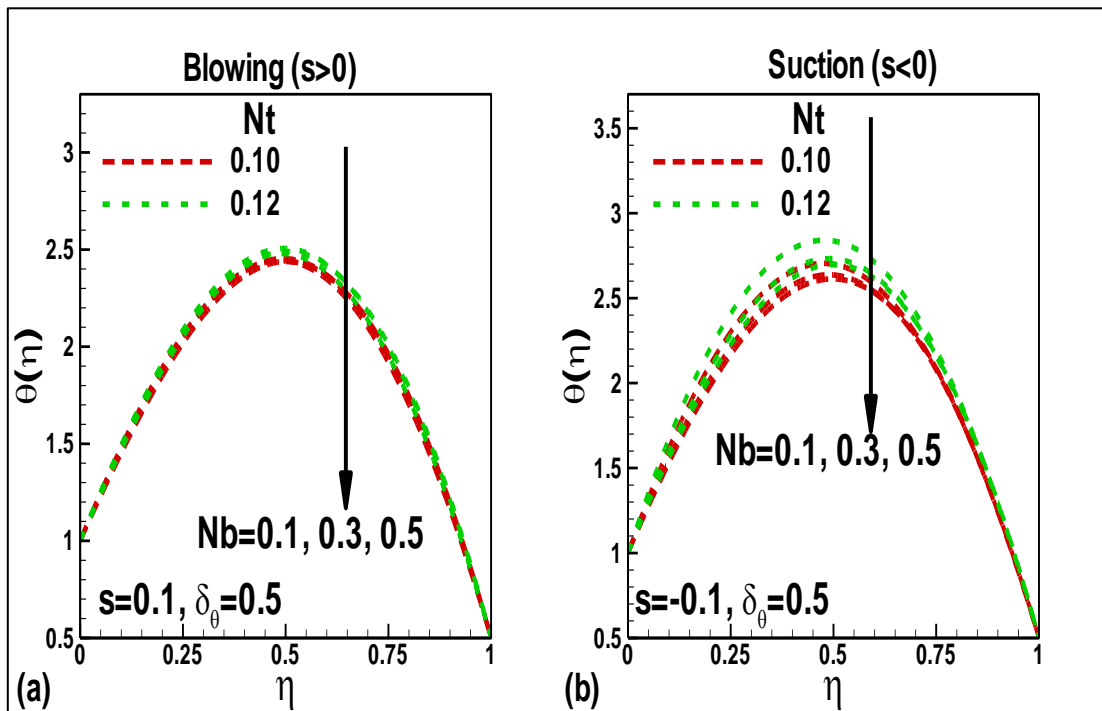
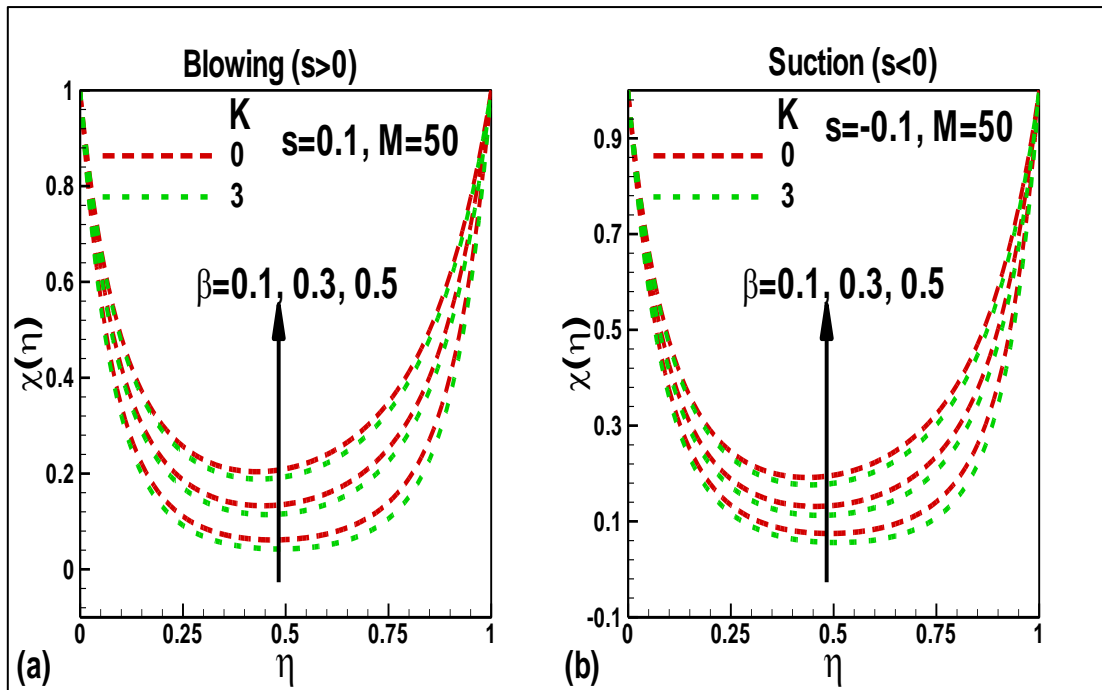


Figure 7: Effects of nanofluid parameters, i.e., thermophoresis parameter (Nt) and Brownian motion parameter (Nb) on dimensionless temperature for a) blowing and b) suction.

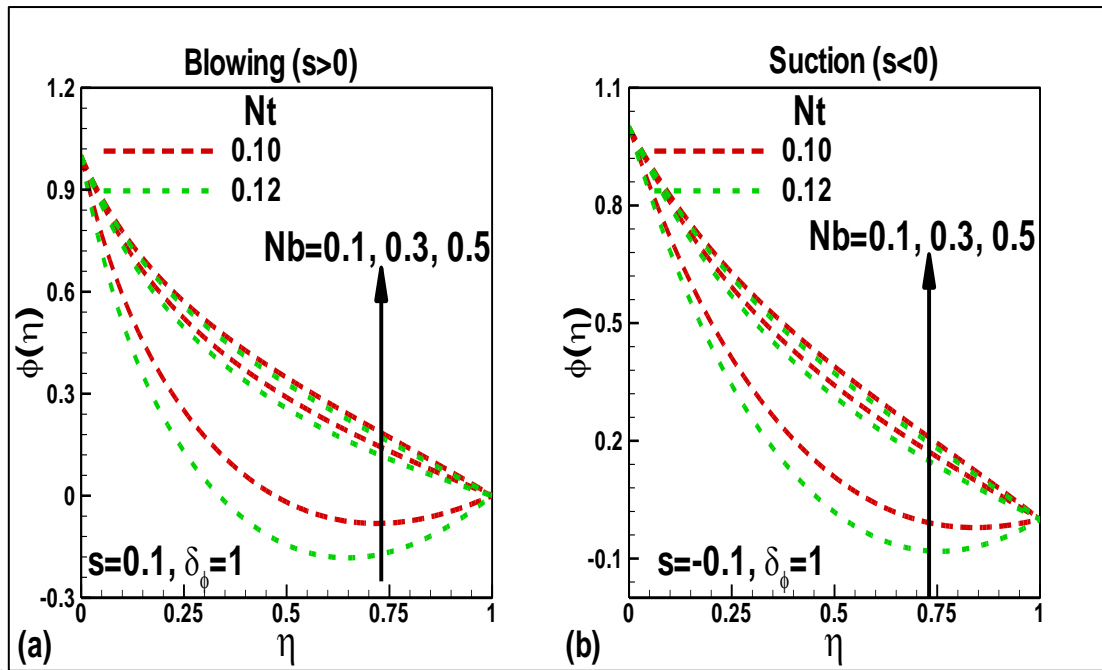


Figure 8: Effects of nanofluid parameters, i.e., thermophoresis parameter (Nt) and Brownian motion parameter (Nb) on dimensionless nanoparticle concentration for a) blowing and b) suction.

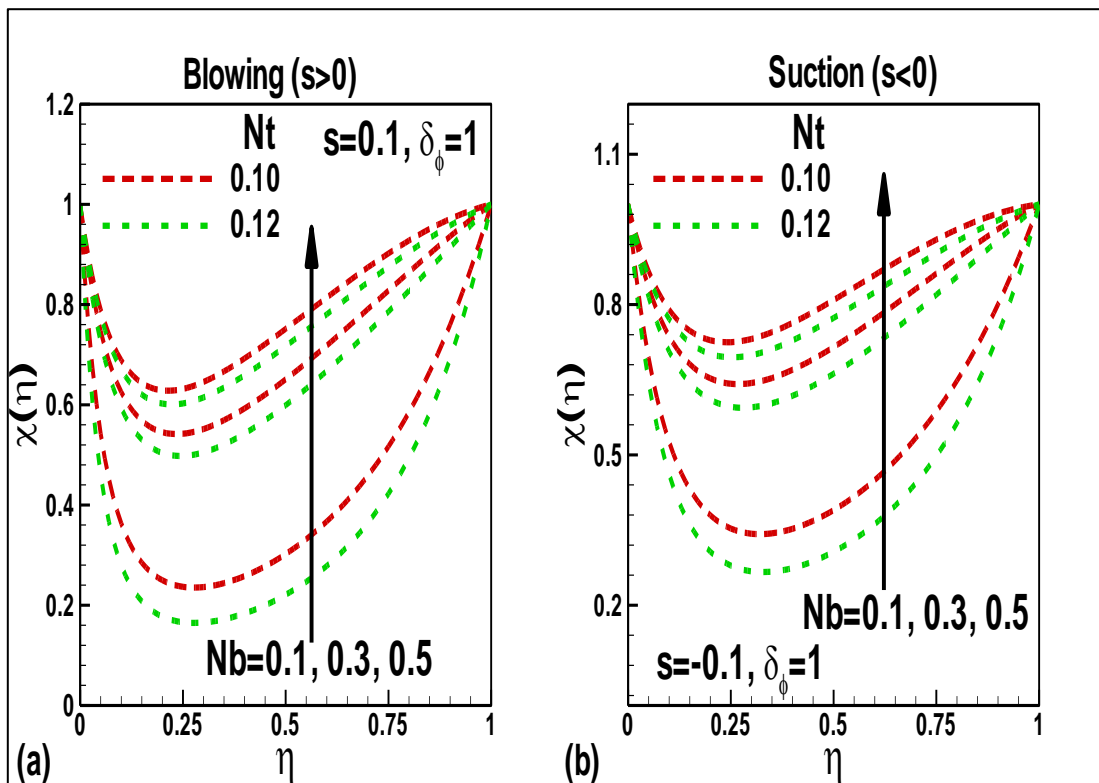


Figure 9: Effects of nanofluid parameters, i.e., thermophoresis parameter (Nt) and Brownian motion parameter (Nb) on dimensionless motile microorganism density number for a) blowing and b) suction.

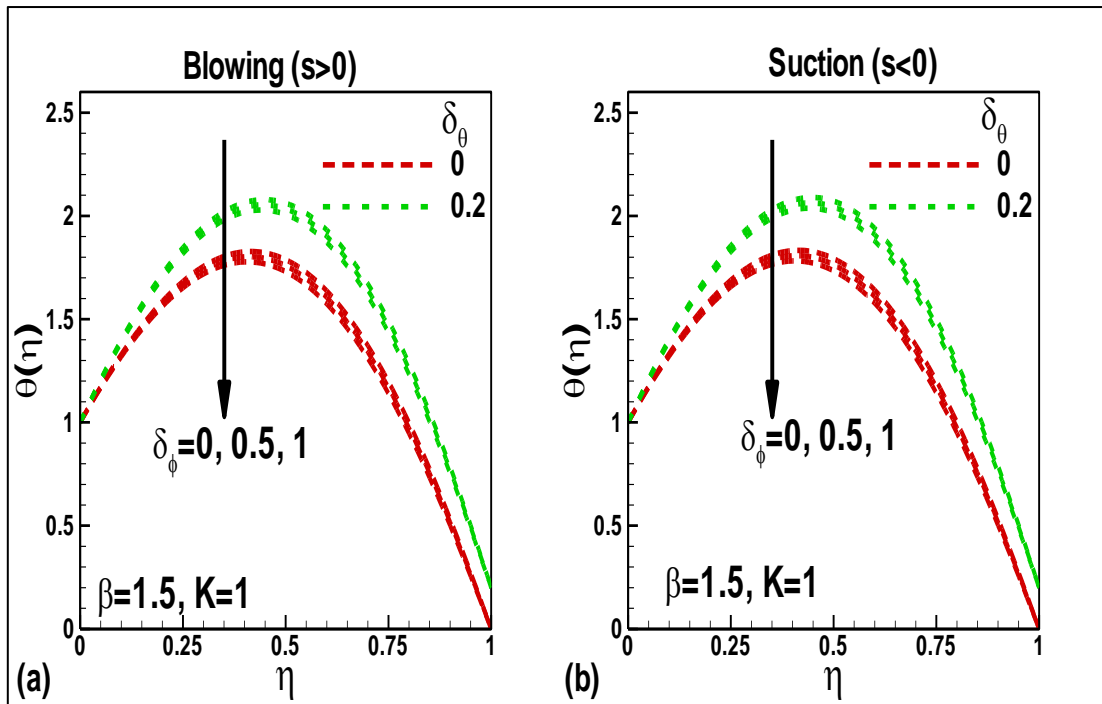


Figure 10: Effects of boundary temperature parameter (δ_θ) and boundary nanoparticle concentration parameter (δ_ϕ) on dimensionless temperature for a) blowing and b) suction.

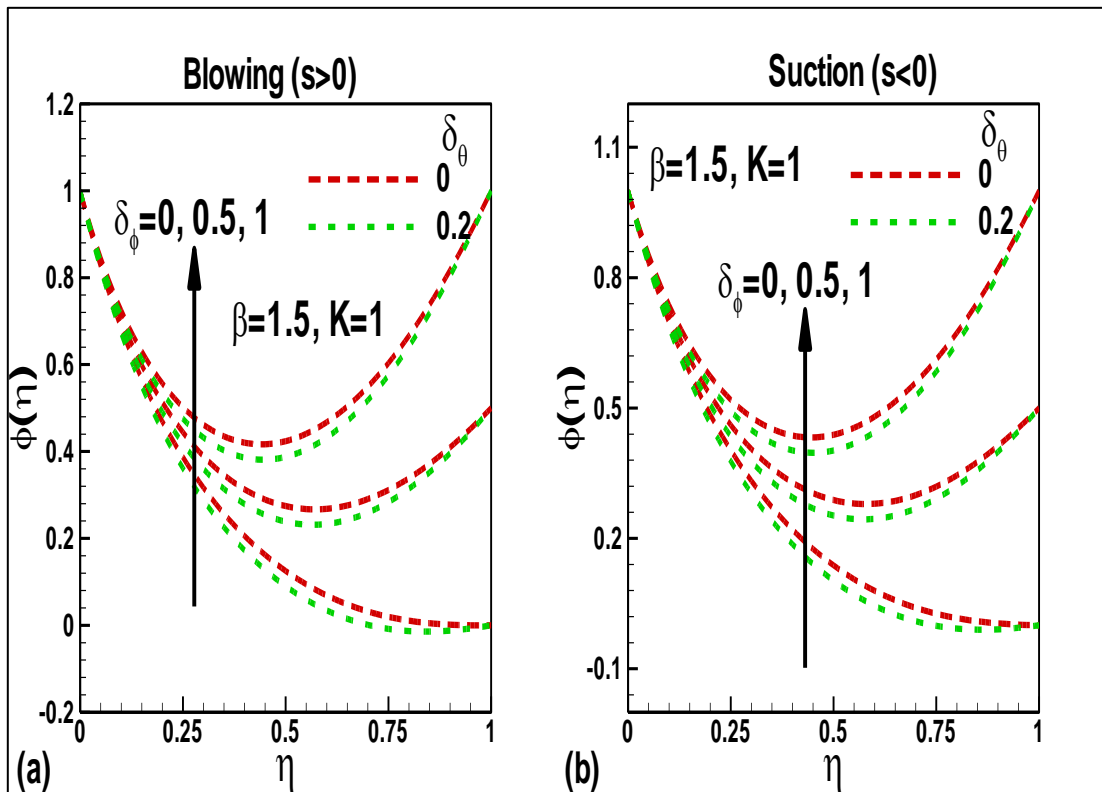


Figure 11: Effects of boundary temperature parameter (δ_θ) and boundary nanoparticle concentration parameter (δ_ϕ) on dimensionless nanoparticle concentration for a) blowing and b) suction.

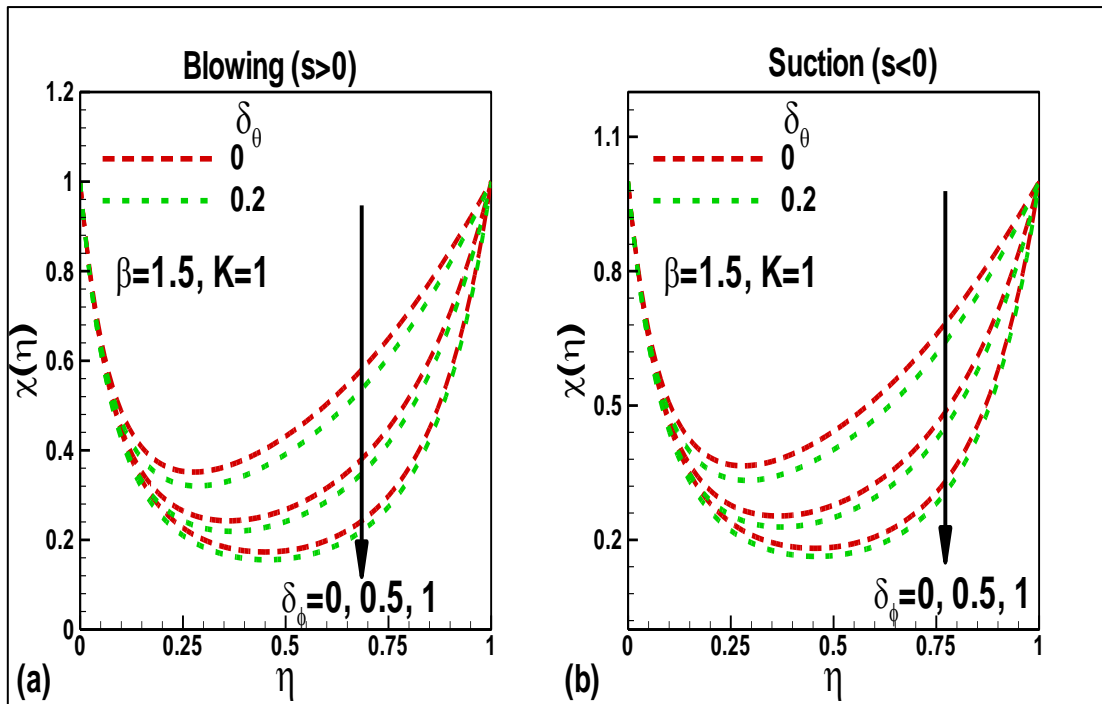


Figure 12: Effects of boundary temperature parameter (δ_θ) and boundary nanoparticle concentration parameter (δ_ϕ) on dimensionless motile microorganism density number for a) blowing and b) suction.

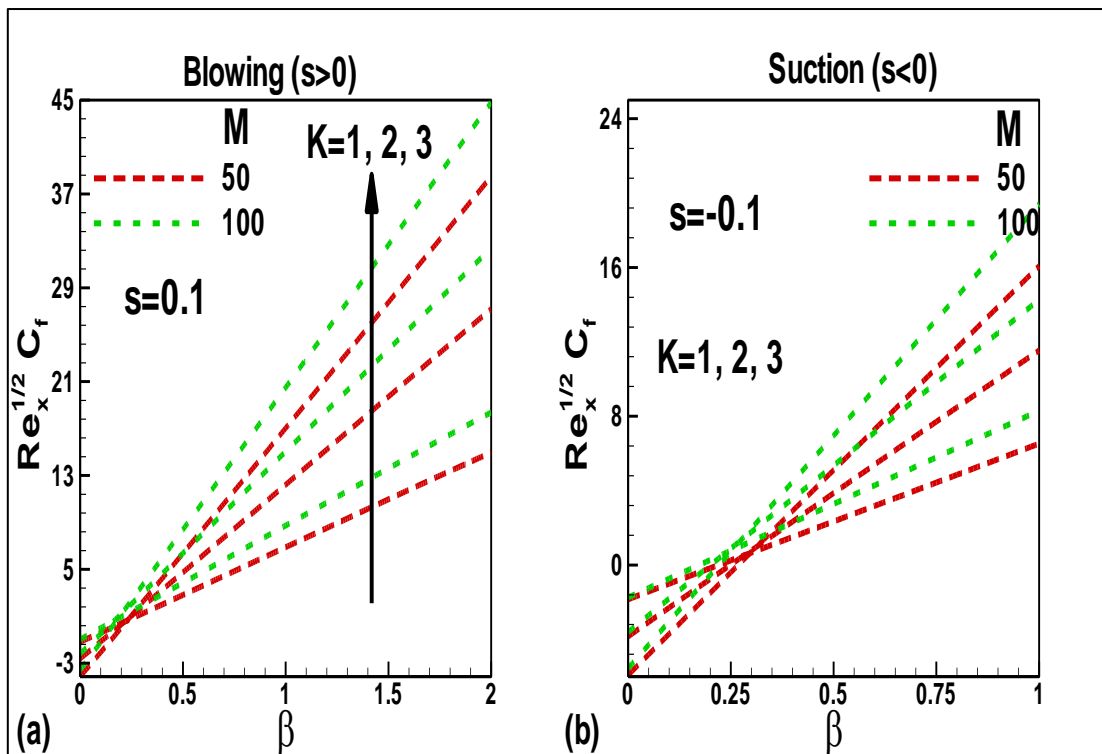


Figure 13: Variation of skin friction with squeeze number (β) for different values of micro rotation parameter (K) and magnetic field parameter (M) for a) blowing and b) suction.

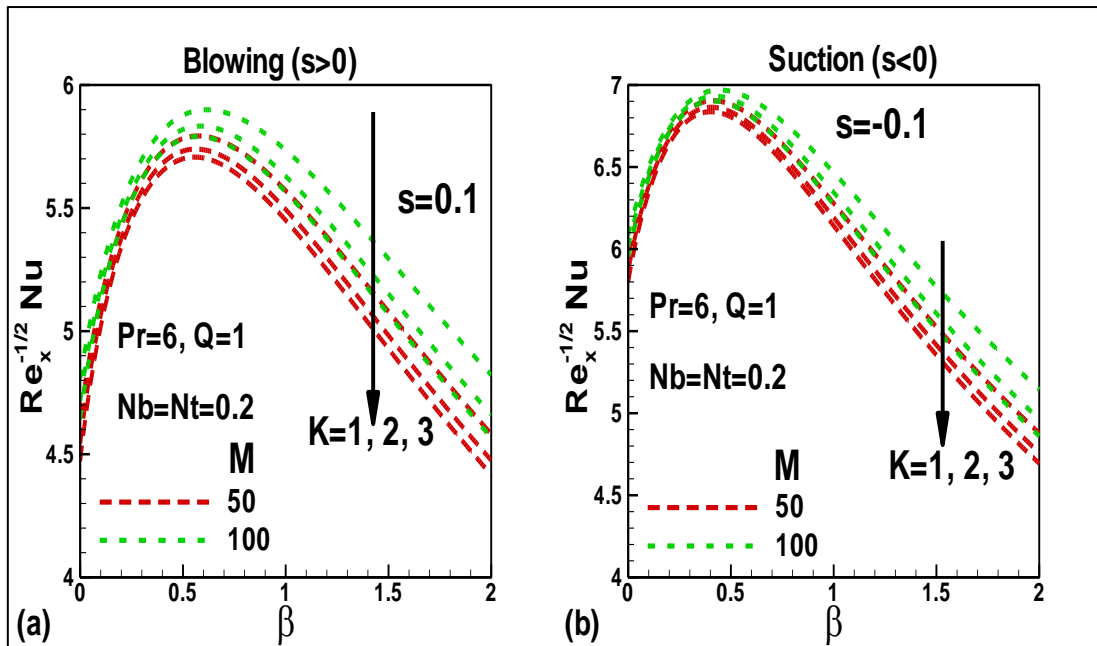


Figure 14: Variation of Nusselt number with squeeze number (β) for different values of micro rotation parameter (K) and magnetic field parameter (M) for a) blowing and b) suction.

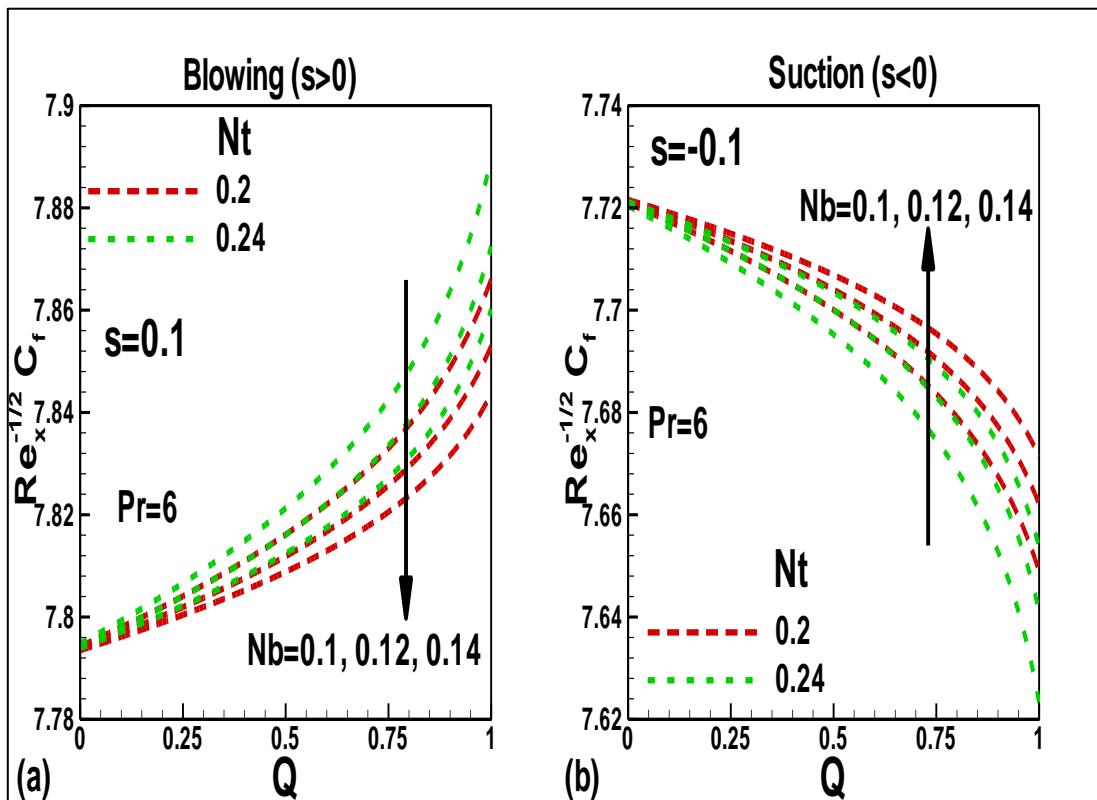


Figure 15: Variation of the skin friction with heat generation parameter (Q) for different values of thermophoresis parameter (Nt) and Brownian motion parameter (Nb) for a) blowing and b) suction.

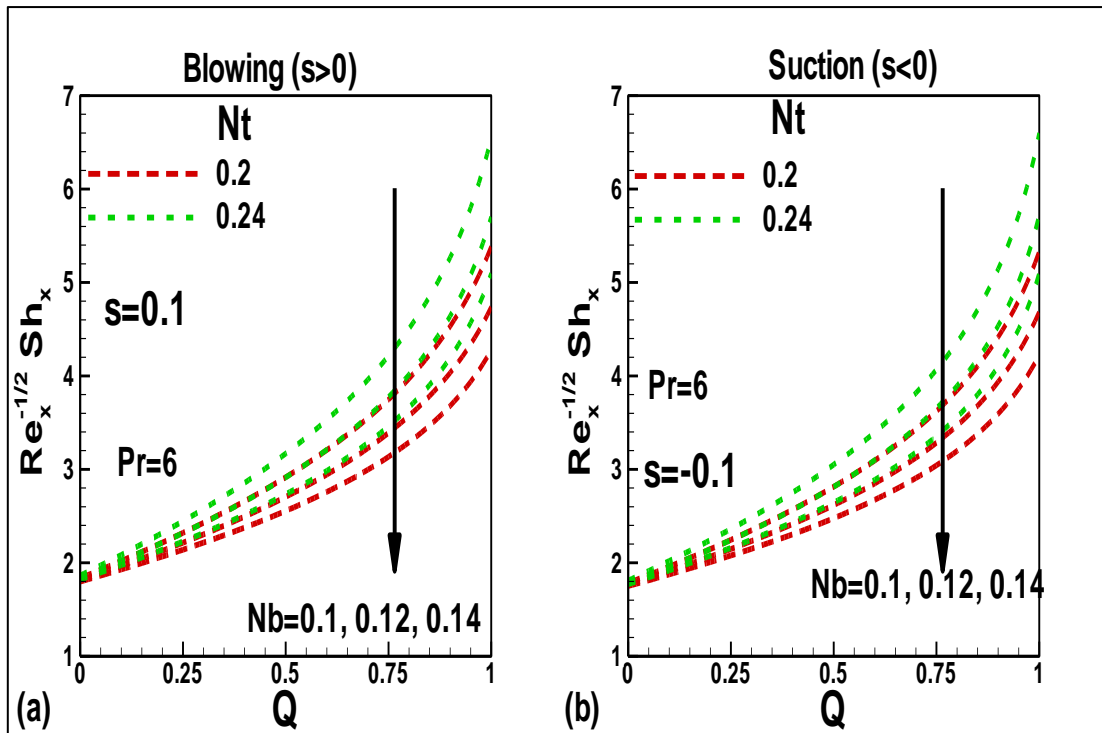


Figure 16: Variation of the nanoparticle Sherwood number with heat generation parameter (Q) for different values of thermophoresis parameter (Nt) and Brownian motion parameter (Nb) for a) blowing and b) suction.

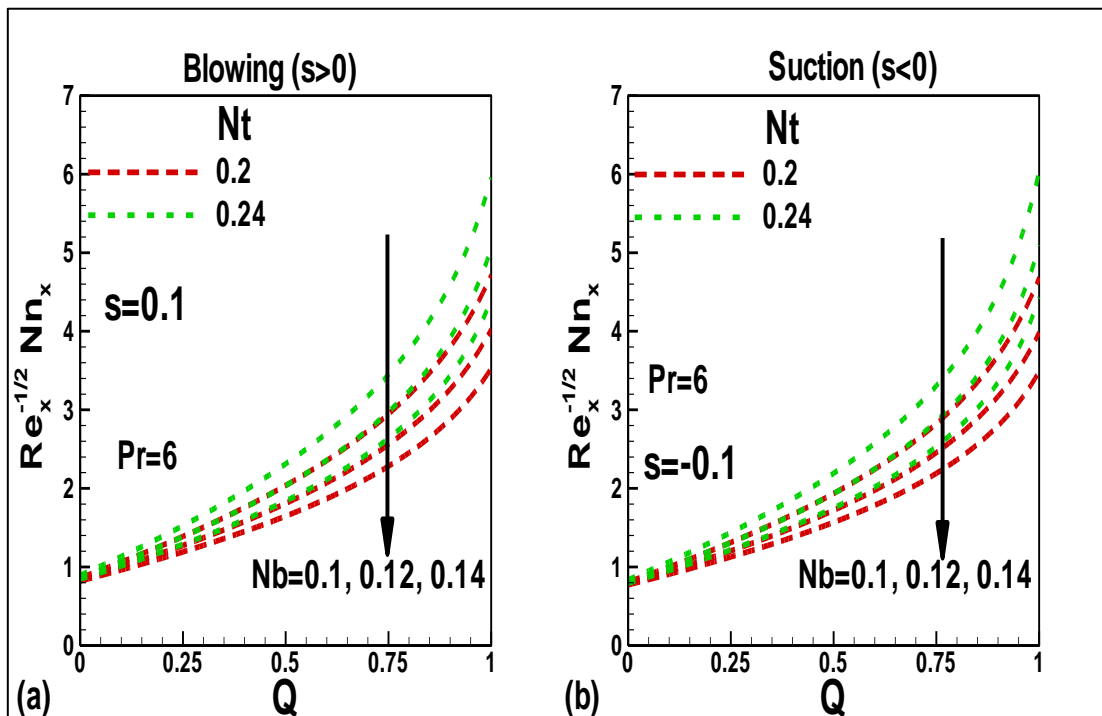


Figure 17: Variation of the local wall motile microorganism density number gradient with heat generation parameter (Q) for different values of thermophoresis parameter (Nt) and Brownian motion parameter (Nb) for a) blowing and b) suction.

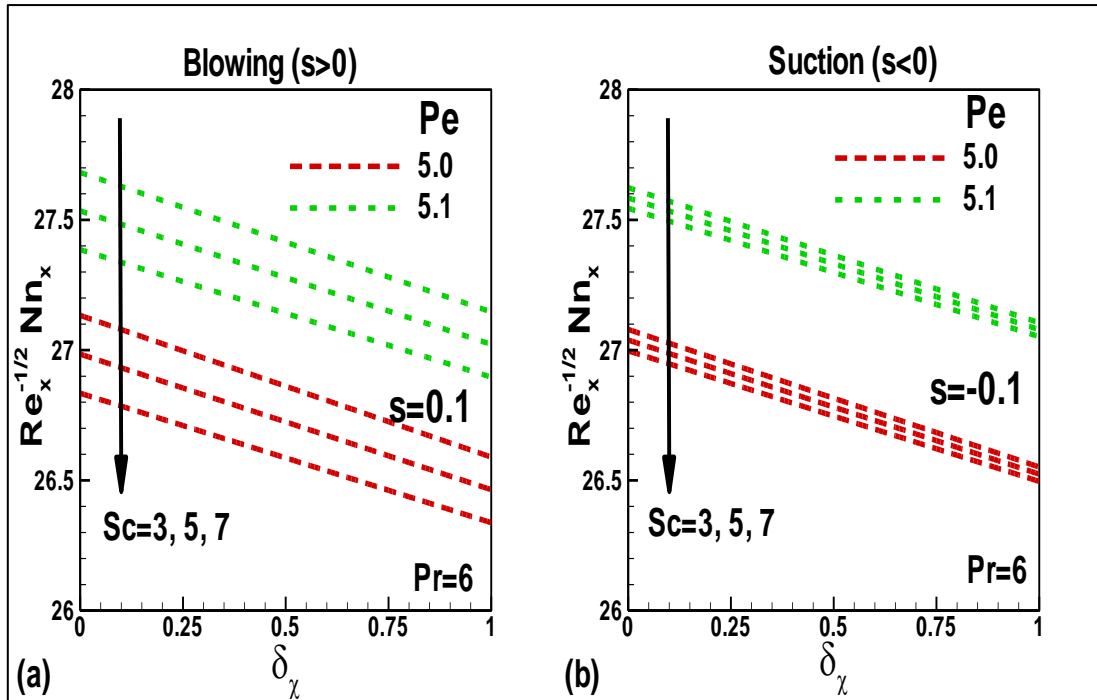


Figure 18: Variation of the local wall motile microorganism density number gradient with microorganism boundary parameter (δ_χ) for different values of bioconvection Péclet number (Pe) and Schmidt number (Sc).

Table 3: Values of the skin friction, local Nusselt number, local nanoparticle Sherwood number, and motile micro-organism wall gradient rate for various parameters.

	Blowing ($s > 0$)				Suction ($s < 0$)			
	$Re_x^{-1/2} C_f$	$Nu_x Re_x^{-1/2}$	$Sh_x Re_x^{-1/2}$	$Nn_x Re_x^{-1/2}$	$Re_x^{-1/2} C_f$	$Nu_x Re_x^{-1/2}$	$Sh_x Re_x^{-1/2}$	$Nn_x Re_x^{-1/2}$
B	$Re_x^{-1/2} C_f$ $\beta = Le = R = Q = \delta_\chi = Sc = Pe = 1, M = 50, Pr = 6, Nb = Nt = l = 0.2, \delta_\phi = 0$							
0	2.6943	2.1034	4.4750	3.7990	1.8927	2.3771	4.0540	3.3863
0.2	2.7009	2.1035	4.4747	3.7987	1.8998	2.3773	4.0538	3.3860
0.4	2.7079	2.1037	4.4744	3.7983	1.9073	2.3775	4.0536	3.3858
0.6	2.7154	2.1039	4.4741	3.7980	1.9154	2.3777	4.0534	3.3855
0.8	2.7233	2.1041	4.4737	3.7976	1.9239	2.3780	4.0531	3.3852
1.0	2.7318	2.1044	4.4733	3.7971	1.9331	2.3782	4.0529	3.3849
R	$\beta = Le = B = R = Q = \delta_\chi = Sc = Pe = 1, M = 50, Pr = 6, Nb = Nt = l = 0.2, \delta_\phi = 0$							
0	2.6258	2.1435	3.5572	2.8619	1.9713	2.3674	3.4160	2.7287
0.2	2.6439	2.1346	3.7516	3.0614	1.9581	2.3693	3.5562	2.8739
0.4	2.6615	2.1262	3.9395	3.2538	1.9456	2.3713	3.6892	3.0112
0.6	2.6786	2.1183	4.1221	3.4401	1.9336	2.3734	3.8159	3.1417
0.8	2.6953	2.1109	4.3001	3.6213	1.9222	2.3755	3.9371	3.2662
1.0	2.7116	2.1038	4.4742	3.7982	1.9113	2.3776	4.0535	3.3856

Figures 2-6 illustrate the impact of microrotation parameter (K) and squeeze number (β) on dimensionless linear velocity, angular velocity, temperature, nanoparticle concentration, and motile microorganism density number for a) blowing and b) suction. **Figure 2** shows that there is a considerable boost in flow velocity with an increment in squeeze number (β) across the gap, i.e., from the lower plate ($\eta = 0$) to the upper plate ($\eta = 1$). Momentum imparted to the squeezing flow produces this acceleration. However, slightly higher velocity magnitudes arise for the blowing case ($s > 0$) relative to the suction case ($s < 0$) since the former induces a momentum boost, whereas the latter produces a strong deceleration effect. In particular, for the low value of squeeze number ($\beta = 0.1$), the velocity profile for the suction case is significantly suppressed, and much greater magnitudes are evident for the blowing case (inverse parabola topology). Peak velocity always arises at the centreline of the gap, i.e., ($\eta = 0.5$). With the increment in the Eringen micropolar parameter (K), the velocity is decreased near the plates but significantly enhanced at the center of the gap for both blowing and suction. The parameter $K = \frac{k_1}{\mu}$ relates the vortex viscosity of the microfluid to the dynamic viscosity.

As this parameter increases the gyratory motions of the micro-elements, this encourages flow acceleration in the regime. When $K = 0$, micropolar effects are negated. Slightly more incredible velocity is computed at the core of the channel (center of gap) with blowing than suction. In all cases, we consider the accelerating plates moving apart, i.e., a relaxation in the squeezing regime. Stronger micropolarity benefits the regime and improves lubrication performance since flow acceleration is achieved. Furthermore, the magnetic parameter is constrained at $M = 50$, indicating a strong applied magnetic field. **Figure 3** indicates that a very different set of profiles is computed for angular velocity (micro-rotation) as compared to linear (translational) velocity shown in Fig. 2. In both suction and blowing cases, angular velocity profiles are observed to be minimal (negative) at the lower plate and ascend to maximum value at the upper plate. The negative values indicate reverse spin, i.e., a re-orientation in the gyration motion of the micro-elements at the lower plate. With more significant values of squeeze number (β), there is a substantial depletion in angular velocity, although this implies a more excellent reverse spin of micro-elements. For $\beta = 0.1$ (*low squeeze number*), there is a linear growth in the blowing case for micro-rotation; however, in the suction case, the profiles remain largely invariant (horizontal). As elaborated earlier, for blowing, $s > 0$, mass is being expelled from the plates, whereas for suction, $s < 0$, mass is being absorbed into the plate surface, and this introduction of extra micropolar nanofluid effectively damps the micro-rotation values. With increasing K values, the micro-rotation is increased significantly, i.e., acceleration is induced in the gyration motions of the micro-elements. **Figure 4** shows that dimensionless temperature is strongly increased with larger

values of the squeeze number (β). In both injection and suction cases, the profiles exhibit inverse parabolic patterns. However, a higher temperature is always attained at the lower plate relative to the upper plate, which experiences more cooling. Peak temperature is always computed at the center of the gap, i.e., $\eta = 0.5$. Significantly higher temperatures are observed in the vicinity of the core zone for the suction case relative to the blowing case. Thermal diffusion in the regime is therefore improved with suction. However, while slightly greater temperatures are produced in the blowing case with an increase in micropolar parameter (K), the reverse effect is computed for the suction case. While the parameter, K , does not feature explicitly in the energy conservation (heat) Eq. (12), via the coupling term, $Pr[+f\theta']$, there is a strong interplay with the micropolar terms in the linear momentum Eq. (10), viz, $-(1 + K)f'''' - Kh''$. The micropolarity effect is therefore indirectly experienced via these coupling terms in the temperature field. Furthermore, Eq. (12) is weakly coupled to the micro-rotation Eq. (11). **Figure 5** shows that nanoparticle concentration (volume fraction) is strongly elevated with an increase in squeeze number (β) for both Stefan blowing and suction cases. For both suction and blowing cases, the profiles are inverse parabolas. There is a weak reduction in nanoparticle concentration with an increment in micropolar parameter (K). Greater micropolar vortex viscosity, therefore slightly inhibits nanoparticle diffusion implying that the non-Newtonian microstructural effect reduces the transport of nanoparticles in the squeezing regime. Again, while K does not feature explicitly in the nanoparticle concentration Eq. (3), the term, $-PrLe[-f\phi']$ produces a coupling with the linear momentum Eq. (10) which does contain the micro-rotation vortex viscosity parameter, K in the term, $-(1 + K)f'''' - Kh''$. There is a slight asymmetry in the profiles for both suction and injection and minimal nanoparticle concentration values are computed slightly off-centre, i.e. to the right of the channel gap centreline. This asymmetry is absent in the linear velocity and angular velocity profiles in Figs 2 and 3. **Figure 6** shows that micro-organism number density is considerably enhanced with elevation in the squeeze number (β). Again, inverted parabolas are computed for both blowing and suction cases, which are generally symmetric about the centreline. Therefore, as the plates move apart, the propulsion of micro-organisms is encouraged. Slightly higher values are computed for the blowing case relative to the suction case. Stefan blowing clearly energizes the regime which in turn boosts the micro-organism density number enabling more efficient swimming. There is however a weak suppression in micro-organism density with increment in micropolar parameter (K). As with the temperature and nanoparticle concentration, K does not feature in the micro-organism density number conservation Eq. (14). However, the term, $+Scf\chi'$ couples Eq. (14) with the linear momentum Eq. (10) which in turn is also coupled strongly to the micro-rotation conservation Eq. (11) via the terms, $+(f'h - fh') + B(2h + f'')$.

Figs. 7-9 depict the impact of the thermophoresis parameter (Nt) and Brownian motion parameter (Nb) for a) blowing and b) suction on selected transport variables. Fig. 7 shows that the temperature values significantly decrease with increasing Brownian motion parameter, for both the Stefan blowing and suction cases. This parameter is featured in both energy Eq. (12) in the term, $Nb\phi'\theta$, and also in the term $+\frac{Nt}{Nb}\theta''$ in the nanoparticle species Eq. (13). Larger values of Nb imply smaller sizes of the nanoparticles in the micropolar nanofluid. As Nb increases, a weak reduction in temperature is produced for both the blowing and suction cases. Peak temperatures arise at the centreline of the gap. Suction produces slightly higher temperatures than blowing. With increasing thermophoretic parameter, Nt , the opposite trend is produced, and temperatures of the micropolar nanofluid are strongly elevated, particularly in the core zone of the gap. The parameter Nt embodies the effect of a temperature gradient driving nanoparticles from hotter to colder regions in the regime. It is a nanoscale effect that encourages heat transfer and warms the regime. Nt arises both in the energy Eq. (12) in the term, $+Nt(\theta')^2$ and also in the coupling term, $+\frac{Nt}{Nb}\theta''$ in the nanoparticle species Eq. (13). Thermal management of the squeezing regime can, therefore, be achieved via adjustment in the nanoscale parameters. **Figure 8** shows that temperature distribution influences the nanoparticle concentration function very differently. While an increase in Brownian motion, Nb , produces a strong elevation in nanoparticle concentration across the gap, at low values of Nb the profiles are monotonic decays from the lower plate to the upper plate, whereas at higher values of Nb they are generally linear decays. Brownian motion encourages ballistic collisions between nanoparticles and enhances species diffusion. A slight increase in nanoparticle concentration values also accompanies an increment in thermophoresis coefficient, Nt , although the effect is more dramatic at lower Brownian dynamics parameter Nb values. Substantially higher magnitudes of nanoparticle concentration are computed for the Stefan blowing case relative to the suction case at all locations across the gap. **Figure 9** demonstrates that the dimensionless motile microorganism density number $\chi(\eta)$ is reduced with an increment in the thermophoresis parameter, Nt , for both a) blowing and b) suction. Peak values always arise at the lower and upper plates, and the minimal values are computed in the lower half-space (to the left of the gap centreline). A significant elevation is, however, induced in motile microorganism density number, $\chi(\eta)$ with an increase in Brownian motion parameter (Nb). The profiles in both the suction and blowing cases are skewed inverted parabolas across the gap. Slightly greater magnitudes appear in the core zone of the two-plate gap geometry for the suction case. While neither nanoscale parameter features in the micro-organism species Eq. (14), there are coupling terms, $-Pe[\chi\phi'' + \phi'\chi']$, linking this

equation to the nanoparticle species Eq. (13). This results in an indirect influence on the propulsion of micro-organisms with both the thermophoresis parameter (Nt) and Brownian motion parameter (Nb). The dynamics of the gyrotactic micro-organisms can effectively be manipulated with nanoscale effects, even though the nanoparticles do not interact directly with the micro-organisms.

Figures 10-12 display the response in selected variables (temperature, nanoparticle concentration and motile micro-organism density number) to a change in the values of the boundary temperature parameter (δ_θ) and boundary nanoparticle concentration parameter (δ_ϕ). Again, both Stefan blowing and suction cases are considered. In both plots we have constrained micropolar parameter as $K = 1$ (equal vortex viscosity and dynamic viscosity) and also consider again the case where the plates are accelerating away from each other ($\beta = 1.5$) so that the gap is increasing. The thermal boundary parameter, $\delta_\theta = \frac{T_1 - T_0}{T_2 - T_0}$ appears only in the upper plate wall temperature boundary condition, Eq. (15) as $\theta(1) = \delta_\theta$ and the nanoparticle boundary parameter, $\delta_\phi = \frac{c_1 - c_0}{c_2 - c_0}$ features in the upper plate wall nanoparticle concentration boundary condition, $\phi(1) = \delta_\phi$ also in Eq. (15). These parameters represent temperature and nanoparticle concentration differences between the two plates. **Figure 10** shows that as δ_θ increases there is a significant boost in temperature across the channel gap. The peak temperature is computed to the left of the gap centre line. Slightly greater temperatures are associated with the suction case relative to the Stefan blowing case. The temperature difference across the gap produces a strong mobilization in thermal convection, elevating temperatures. With greater δ_θ However, there is a strong decrease in temperature. Greater nanoparticle concentration difference across the gap impedes heat diffusion, which can be exploited as a mechanism for thermal control in squeezing lubrication systems. **Figure 11** reveals that with increasing boundary temperature parameters (δ_θ) there is a noticeable reduction in nanoparticle concentration across the gap. Profiles initially decay from the lower plate but then ascend to the upper plate. Minimum nanoparticle concentration magnitudes always arise at the upper plate for both Stefan blowing and suction cases when the nanoparticle concentration boundary parameter (δ_ϕ) vanishes i.e. $\delta_\phi = 0$. As δ_ϕ increases the disparity between nanoparticle concentrations across the gap and intensifies it. This encourages the transport of nanoparticles in the gap regime and boosts their values substantially. In the Stefan blowing case ($s > 0$), larger magnitudes are computed in nanoparticle concentration. The distribution of nanoparticles within the magnetized micropolar nanofluid lubricant can, therefore, be manipulated successfully with modification in the nanoparticle concentration boundary parameter (δ_ϕ), which, in turn, will

enhance the load capacity of the lubricant. **Figure 12** shows that dimensionless motile microorganism density number is also influenced significantly by a modification in both boundary temperature parameter (δ_θ) and boundary nanoparticle concentration parameter (δ_ϕ). These parameters are not featured in the micro-organism wall boundary condition at the upper plate via strong coupling of the micro-organism species conservation equation (14) to the nanoparticle species Eq. (13) through the terms, $'-Pe[\chi\phi'' + \phi'\chi']$ and further coupling between the nanoparticle species Eq. (13) and the temperature Eq. (12), via the term, $+\frac{Nt}{Nb}\theta''$, there is an indirect effect produced on the micro-organism number density field. With an increment in boundary temperature parameter (δ_θ) The micro-organism density number is suppressed across the gap, with the most dramatic influence focused on the central zone. Slightly higher magnitudes are associated with the suction case. With larger values of nanoparticle concentration boundary parameters (δ_ϕ) There is also a depletion computed in micro-organism density number, $\chi(\eta)$ which is sustained across the entire gap from the lower to the upper plate. Peak values in micro-organism density numbers $\chi(\eta)$ always arise at both boundaries (plates), and values plummet to a minimum at the center line of the gap. Therefore, the propulsion of micro-organisms in the lubrication gap is significantly damped by the increasing nanoparticle concentration difference imposed between the two boundaries. The motion of the micro-organisms (bioconvection) can, therefore, demonstrably be altered via manipulation of the nanoparticle concentration boundary parameter (δ_ϕ) which in turn can be utilized to modify the load capacity of the system.

Figures 13-18 illustrate the impact of selected parameters on several wall gradient characteristics, i.e., skin friction, Nusselt number, nanoparticle Sherwood number, and wall motile microorganism density number gradient again for the Stefan blowing and suction cases. **Figure 13** shows that a linear relationship is computed between skin friction and increasing squeeze number (β). Since the plates are accelerating apart for larger values of this parameter, the squeezing phenomenon is reduced, and the flow accelerates at the lower plate, i.e., the magnetic micropolar nanofluid shears faster along the lower plate. Skin friction is considerably boosted with an increment in the micropolar vortex viscosity parameter (K). The lubricant flow is accelerated, confirming the drag-reducing properties of microstructural characteristics [20-23]. With an increment in the magnetic field parameter, M , the skin friction is generally enhanced at all values of squeeze number. Magnetic field intensification accelerates the flow since the plates are moving apart and not towards each other, i.e., it produces the opposite effect of damping. This pattern is computed for both the Stefan blowing and suction scenarios, although only after a critical squeeze number is attained. In the linear momentum Eq. (10), the magnetic body force, $+Mf''$, is assistive to

momentum development and not inhibiting. This manifests in the strong flow acceleration observed, i.e., the enhancement in skin friction at the lower plate boundary. Significantly higher skin friction values are computed for the Stefan blowing case relative to the suction case at all values of the magnetic parameter, micropolar parameter, or squeeze number. **Figure 14** shows the influence of squeeze number (β) for different values of micro rotation parameter (K) and magnetic field parameter (M) for a) blowing and b) suction on Nusselt number, i.e., heat transfer gradient at the lower plate. A strong reduction in Nusselt number is produced with increasing micropolar vortex viscosity parameter (K). While temperatures within the gap are enhanced, the net rate of heat flow to the lower plate boundary is reduced. This implies that the micropolarity of the nanofluid can be beneficial in the thermal management of the boundary where cooling mitigates the onset of possible high-temperature corrosion effects. Slightly higher Nusselt numbers are computed for the suction case. With an increment in squeeze number, there is an initial climb in Nusselt numbers. However, this peak quickly, and thereafter, values decay with subsequent increases in the squeeze number. The implication is that a critical squeeze number ($\beta \sim 0.5$) exists up to which heat transfer to the wall is boosted. However, beyond this value, owing to a much wider gap between the plates that are separating for positive squeeze number, the heat convected to the lower plate is suppressed, manifesting in a depletion in the Nusselt number. Therefore, the minimum Nusselt number is computed for the largest value of the squeeze number ($\beta = 2$). With increasing magnetic parameter, $M = \frac{\sigma B^2(1-at)}{\rho b}$, there is a clear elevation in Nusselt number. Since

flow acceleration is produced with the stronger magnetic field, less work is expended by the magnetic micropolar nanofluid. This leads to a cooling effect within the regime, and the net heat flux is away from the lubricant and towards the lower plate. This elevates the Nusselt number at the lower boundary (plate). **Figure 15** shows skin friction grows strongly with the heat generation parameter (Q). In other words, an intensifying heat source energizes the regime, encourages thermal convection, and accelerates the shearing of the magnetic micropolar nanofluid lubricant along the lower plate boundary. For the Stefan blowing case ($s=0.1$), increasing the thermophoresis parameter (Nt) elevates the skin friction (flow acceleration at the lower plate) at all values of the heat source parameter, Q . In contrast, an increase in Brownian motion parameter (Nb) produces the opposite effect, i.e., flow deceleration at the lower plate. Overall, maximum skin friction is associated with the maximum heat source parameter, maximum thermophoresis parameter, and minimal Brownian motion parameter. Conversely, for the suction case ($s = -0.1$), for which micropolar nanofluid is being absorbed into the surface (e.g., micropolar nanofluid suction),

increasing Brownian motion parameter (Nb) enhances skin friction (flow acceleration at the lower plate) whereas greater values of heat source parameter, Q and thermophoresis parameter (Nt) strongly suppress skin friction (flow retardation at the lower plate). The topologies for Stefan blowing and suction are also very different. In the former, they are monotonic growths with heat source parameter Q , whereas in the latter, they are monotonic decays. Clearly, the presence of Stefan blowing or suction profoundly affects skin friction characteristics, nanoscale parameters, and heat source effect. **Figure 16** illustrates that the nanoparticle Sherwood number is consistently enhanced with increment in heat generation parameter (Q) for both a) Stefan blowing and b) suction. The thermal energy generation via the heat source effect encourages nanoparticle diffusion to the lower boundary irrespective of suction or blowing. An increase in Brownian motion parameter (Nb), however, induces a strong depletion in nanoparticle Sherwood number magnitudes. Conversely, increasing the thermophoresis parameter (Nt) leads to a significant enhancement in nanoparticle Sherwood number. The thermal gradient driving the nanoparticles from cooler zones to hotter zones encourages nanoparticle species diffusion to the lower plate. However, the Brownian motion effect has the reverse influence and decreases nanoparticle transport to the lower boundary.

Figure 17 depicts the evolution in local wall motile microorganism density number gradient with heat generation parameter (Q) for different values of thermophoresis parameter (Nt) and Brownian motion parameter (Nb) for a) blowing and b) suction. With either Stefan blowing or suction present, there is a steady escalation in wall motile microorganism density number gradient with increasing heat source parameter values. The internal heat generation therefore significantly assists the propulsion of micro-organisms towards the lower plate. Conversely higher values of Brownian motion parameter (Nb) lead to a significant reduction in wall motile microorganism density number gradient and oppose the swimming motions of the micro-organisms towards the lower plate. Smaller nanoparticles are therefore counter-productive for propulsion of micro-organisms towards the boundary whereas larger nanoparticles (smaller Nb values) will produce the opposite effect. With increasing thermophoresis parameter (Nt), whether Stefan blowing or suction is present, the wall motile microorganism density number gradient is boosted considerably. Propulsion of micro-organisms is therefore strongly enhanced towards the lower plate. Again, it is evident that nanoscale parameters in the magnetized micropolar nanofluid lubricant can be adjusted to induce modifications in the swimming dynamics of the gyrotactic micro-organisms.

Finally, **Figure 18** indicates that local wall motile microorganism density number gradient is significantly reduced with an elevation in microorganism boundary parameter (δ_χ). Similar to the other thermal and nanoparticle species boundary parameters examined earlier, the micro-organism boundary parameter, $\delta_\chi = \frac{n_1 - n_0}{n_2 - n_0}$, embodies the effect of different micro-organism density numbers across the gap. It also arises in the upper plate boundary condition, Eq. (15) as $\chi(1) = \delta_\chi$. This upper plate boundary condition will exert an influence also on the transport of micro-organisms via Eq. (14) and in turn the propulsion of micro-organisms to the lower plate. Generally linear decays are computed with increasing microorganism boundary parameter (δ_χ) for both Stefan blowing or suction conditions. Similar magnitudes are computed. With an increment in bioconvection Péclet number (Pe) however there is a substantial boost in local wall motile microorganism density number gradient at the lower plate. This is a critical parameter regulating the swimming motions of the micro-organisms. It appears in the term, $-Pe[\chi\phi'' + \phi'\chi']$ in the micro-organism density conservation Eq. (14). $Pe = \frac{\bar{b}W_c}{D_n}$ and expresses the relative swimming speed effect to the micro-organism diffusion effect. Even a slight increase in bioconvection Péclet number (Pe) produces a substantial boost to micro-organism swimming. This results in an accentuation in micro-organisms moving towards the lower plate and the associated elevation in local wall motile microorganism density number gradient at the lower plate, at any value of the microorganism boundary parameter (δ_χ) and for both cases of Stefan blowing and suction. Conversely an increase in bioconvection Schmidt number (Sc) produces a significant suppression in local wall motile microorganism density number gradient at the lower plate. This is sustained for either Stefan blowing or suction. Sc arises only in the micro-organism density number conservation Eq. (14), in the terms, $-Sc\beta\eta\chi'$ and $+Scf\chi'$. $Sc = \nu/D_n$ and expresses the relative rates of momentum diffusion to microorganism species diffusivity in the regime. Since in all cases $Sc > 1$, the momentum diffusion rate exceeds the micro-organism species diffusion rate. This effect is greatest for $Sc = 7$ wherein the momentum diffusivity is seven times the micro-organism diffusivity. This decreases the net migration of swimming gyrotactic micro-organisms towards the lower plate and reduces local wall motile microorganism density number gradient at the lower plate.

Table 3 documents the microinertia density parameter's impact, B , first-order chemical reaction, R on skin friction, local Nusselt, nanoparticle volume fraction, Sherwood, and motile micro-organism density numbers at the lower plate. An increase in microinertia density parameter B , strongly enhances skin friction for both suction and Stefan blowing. However, much higher

magnitudes are computed for the blowing case. $B = \frac{k_1}{\rho j_0 b}$ and arise in one of the coupling terms, $+B(2h + f'')$ in the micro-rotation Eq. (11). Larger values of this parameter indicate a greater spin effect owing to larger microinertia of the micro-elements. This encourages flow acceleration and boosts skin friction. Nusselt number is weakly increased with greater microinertia density parameter, B , and this response is consistently observed for both Stefan blowing and suction. Both the nanoparticle Sherwood number and local wall motile microorganism density number gradient are depleted for Stefan blowing and suction with a greater microinertia density parameter, B . Notably, for all these cases, the squeezing number is positive, i.e., plates are accelerating away from each other. Increasing first-order chemical reaction, R considerably elevates skin friction for the Stefan blowing case and reduces skin friction for the suction case. Conversely, the Nusselt number is reduced with the chemical reaction parameter, R , for the blowing case but increased for the suction case. There is considerable enhancement in the nanoparticle Sherwood number and motile micro-organism wall gradient rate with greater R values for both Stefan blowing and suction present. $R = \frac{c(t)(1-at)}{b}$ and arises only in the nanoparticle species conservation Eq. (13), via the term, $-PrLe[R\phi]$. It represents a homogenous destructive chemical reaction in which nanoparticle species are converted to a different species in the squeezing regime. This produces the decrement in original nanoparticle species within the gap but encourages net diffusion of nanoparticles to the lower plate, resulting in a larger nanoparticle Sherwood number.

8. CONCLUSIONS

This study presents a comprehensive numerical investigation of unsteady, magnetohydrodynamic (MHD), chemically reactive bioconvective micropolar Buongiorno nanofluid squeezing flow between two parallel plates, incorporating Stefan blowing and heat source effects. The model captures multiple physical phenomena, including gyrotactic microorganism bioconvection, nanoparticle diffusion, micro-rotation effects, and thermal generation. Using a robust 4th-5th order Runge-Kutta-Fehlberg method within Maple 24 symbolic software, the coupled nonlinear similarity equations were solved, and the influence of key parameters on velocity, angular velocity, temperature, nanoparticle concentration, and motile microorganism density was analyzed. The key findings are summarized below:

- Skin friction increases with higher micro-rotation parameter (K) and squeeze number (S) for Stefan blowing and suction cases.

- Nusselt number is enhanced by increasing magnetic field strength (M) but decreases with higher micro-rotation (K) and squeeze number (S) when plates are accelerating apart.
- Nanoparticle volume fraction (NPVF) and temperature significantly increase with the squeeze number under blowing and suction conditions.
- Motile microorganism density experiences a slight increase with squeeze number but is reduced with higher micro-rotation and nanoparticle boundary conditions.
- Increasing the microinertia density parameter (B) enhances flow acceleration and skin friction but reduces the nanoparticle Sherwood number and microorganism density gradient at the lower plate.
- Larger values of the chemical reaction parameter (R) boost skin friction and species diffusion (Sherwood number) in the Stefan blowing case but reduce skin friction and Nusselt number under suction.
- Higher values of the thermophoresis parameter (N_t) increase skin friction and nanoparticle diffusion but reduce microorganism density; the Brownian motion parameter (N_b) has the opposite effect, reducing skin friction and promoting nanoparticle and microorganism transport.

9. FUTURE PATHWAYS:

Future investigations can extend the present analysis by incorporating magnetic induction effects and including a magnetic induction conservation equation, which was neglected under the assumption of a low magnetic Reynolds number in the current study. Additionally, employing the Tiwari-Das nanofluid model would allow for considering specific nanoparticle materials and their varying volume fractions, enabling more precise simulations tailored to particular industrial applications. Exploring non-Newtonian models beyond the micropolar framework, such as viscoplastic or viscoelastic models, could further enhance the study's relevance for complex lubricant formulations. Moreover, extending the model to three-dimensional configurations and transient conditions may provide deeper insights into practical bio-nano-tribological systems. Finally, experimental validation of the numerical predictions under laboratory conditions would significantly strengthen the practical applicability of the findings in innovative lubrication technologies and bio-inspired thermal management systems.

REFERENCES

- [1] G.W. Sutton AS. Engineering Magnetohydrodynamics. MacGraw-Hill, New York, USA 1965.

- [2] Zhao Hai C, Wang Y Q. Friction performance analysis of lubricated coated gear with magnetic fluid in CNC machine tools. *Manufacturing Technology and Machine Tools*. 2021; 12:127-31.
- [3] Sun L, Zhang Y, Cui X, An Q, Chen Y, Jia D, et al. Magnetic lubricants: preparation, physical mechanism, and application. *Friction*. 2024.
- [4] Wang Z-L. Research on magnetic fluid lubrication and sealing of rolling bearings. *Tribology*. 2005; 25:88-91.
- [5] Stefan MJ. Versuch über die scheinbare Adhäsion. *Sitzungsber Abt II Österr Akad Wiss Math-Naturwiss Kl*. 1874;69.
- [6] Archibald F. Load capacity and time relations for squeeze films. *Transactions of the American Society of Mechanical Engineers*. 1956;78:29-35.
- [7] Yinusa A, Sobamowo M, Usman M, Abubakar E. Exploration of three dimensional squeezed flow and heat transfer through a rotating channel with coupled Dufour and Soret influences. *Thermal Science and Engineering Progress*. 2021;21:100788.
- [8] Zueco J, Bég OA. Network numerical analysis of hydromagnetic squeeze film flow dynamics between two parallel rotating disks with induced magnetic field effects. *Tribology International*. 2010;43:532-43.
- [9] Bég OA, Tripathi D, Sochi T, Gupta P. Adomian decomposition method (ADM) simulation of magneto-bio-tribological squeeze film with magnetic induction effects. *Journal of Mechanics in Medicine and Biology*. 2015;15:1550072.
- [10] Shamshuddin M, Mishra S, Bég OA, Kadir A. Viscous dissipation and Joule heating effects in non-Fourier MHD squeezing flow, heat and mass transfer between Riga plates with thermal radiation: variational parameter method solutions. *Arabian Journal for Science and Engineering*. 2019;44:8053-66.
- [11] Prakash J, Tripathi D, Bég OA, Sharma RK. Electroosmotic modulated unsteady squeezing flow with temperature-dependent thermal conductivity, electric and magnetic field effects. *Journal of Physics: Condensed Matter*. 2022;34:175701.
- [12] Balaji R, Prakash J, Tripathi D, Bég OA. Computation of magnetohydrodynamic electro-osmotic modulated rotating squeezing flow with zeta potential effects. *Colloids and Surfaces A: Physicochemical and Engineering Aspects*. 2022;640:128430.

- [13] Ren G, Zhou C, Wang S, Fan X, Han Y, Jin G. Improving the rheological and tribological properties of lithium complex grease via complexing agent. *Tribology International*. 2022;175:107826.
- [14] Dang RK, Goyal D, Chauhan A, Dhami S. Effect of non-Newtonian lubricants on static and dynamic characteristics of journal bearings. *Materials Today: Proceedings*. 2020;28:1345-9.
- [15] Wang X-L, Zhu K-Q, Wen S-Z. Thermohydrodynamic analysis of journal bearings lubricated with couple stress fluids. *Tribology international*. 2001;34:335-43.
- [16] Mekheimer KS, Abbas W, Ghazy M, Moawad A, Abo-Elkhair R. Unsteady squeezing Casson fluid through rotating discs under the variable magnetic field, cross diffusion and chemical reaction effects. *International Journal of Modern Physics B*. 2024;38:2450201.
- [17] Wang H, Bi C, Liu W, Zhou F. Squeeze behaviors of magnetorheological fluids under different compressive speeds. *Materials*. 2023;16:3109.
- [18] Hayat T, Yousaf A, Mustafa M, Obaidat S. MHD squeezing flow of second-grade fluid between two parallel disks. *International journal for numerical methods in fluids*. 2012;69:399-410.
- [19] Muhammed RK, Basha H, Reddy GJ, Shankar U, Bég OA. Influence of variable thermal conductivity and dissipation on magnetic Carreau fluid flow along a micro-cantilever sensor in a squeezing regime. *Waves in Random and Complex Media*. 2022:1-30.
- [20] Eringen AC. Theory of micropolar fluids. *Journal of mathematics and Mechanics*. 1966:1-18.
- [21] Dhawan R, Verma S. Analyzing micropolar lubrication in noncircular hybrid journal bearings. *Tribology Transactions*. 2014;57:182-9.
- [22] Nair KP, Nair VS, Jayadas N. Static and dynamic analysis of elastohydrodynamic elliptical journal bearing with micropolar lubricant. *Tribology International*. 2007;40:297-305.
- [23] Hayat T, Nawaz M, Hendi AA, Asghar S. MHD squeezing flow of a micropolar fluid between parallel disks. 2011.
- [24] Bég OA, Rashidi M, Bég TA, Asadi M. Homotopy analysis of transient magneto-bio-fluid dynamics of micropolar squeeze film in a porous medium: a model for magneto-bio-rheological lubrication. *Journal of Mechanics in Medicine and Biology*. 2012;12:1250051.
- [25] Choi SU, Eastman JA. Enhancing thermal conductivity of fluids with nanoparticles. Argonne National Lab.(ANL), Argonne, IL (United States); 1995.

- [26] Wang B, Qiu F, Barber GC, Zou Q, Wang J, Guo S, et al. Role of nano-sized materials as lubricant additives in friction and wear reduction: A review. *Wear*. 2022;490:204206.
- [27] Choi Y, Lee C, Hwang Y, Park M, Lee J, Choi C, et al. Tribological behavior of copper nanoparticles as additives in oil. *Current Applied Physics*. 2009;9:e124-e7.
- [28] Wang Y, Li C, Zhang Y, Li B, Yang M, Zhang X, et al. Comparative evaluation of the lubricating properties of vegetable-oil-based nanofluids between frictional test and grinding experiment. *Journal of Manufacturing Processes*. 2017;26:94-104.
- [29] Rashid U, Abdeljawad T, Liang H, Iqbal A, Abbas M, Siddiqui MJ. The shape effect of gold nanoparticles on squeezing nanofluid flow and heat transfer between parallel plates. *Mathematical Problems in Engineering*. 2020;2020:9584854.
- [30] Ahmad S, Khan MI, Hayat T, Khan MI, Alsaedi A. Entropy generation optimization and unsteady squeezing flow of viscous fluid with five different shapes of nanoparticles. *Colloids and Surfaces A: Physicochemical and Engineering Aspects*. 2018;554:197-210.
- [31] Hayat T, Sajjad R, Alsaedi A, Muhammad T, Ellahi R. On squeezed flow of couple stress nanofluid between two parallel plates. *Results in physics*. 2017;7:553-61.
- [32] Bég OA, Sohail A, Kadir A, Bég T. B-spline collocation simulation of nonlinear transient magnetic nanobio-tribological squeeze-film flow. *Journal of Mechanics in Medicine and Biology*. 2018;18:1850007.
- [33] Ramesh G, Roopa G, Rauf A, Shehzad S, Abbasi F. Time-dependent squeezing flow of Casson-micropolar nanofluid with injection/suction and slip effects. *International Communications in Heat and Mass Transfer*. 2021;126:105470.
- [34] Umavathi J, Patil SL, Mahanthesh B, Bég OA. Unsteady squeezing flow of a magnetized nanolubricant between parallel disks with Robin boundary conditions. *Proceedings of the Institution of Mechanical Engineers, Part N: Journal of Nanomaterials, Nanoengineering and Nanosystems*. 2021;235:67-81.
- [35] Khashi'ie NS, Waini I, Arifin NM, Pop I. Unsteady squeezing flow of Cu-Al₂O₃/water hybrid nanofluid in a horizontal channel with magnetic field. *Scientific Reports*. 2021;11:14128.
- [36] Shankar U, Naduvinamani NB. Magnetized impacts of Brownian motion and thermophoresis on unsteady squeezing flow of nanofluid between two parallel plates with chemical reaction and Joule heating. *Heat Transfer—Asian Research*. 2019;48:4174-202.

- [37] Vincent R, Hill N. Bioconvection in a suspension of phototactic algae. *Journal of Fluid Mechanics*. 1996;327:343-71.
- [38] Plesset MS, Winet H. Bioconvection patterns in swimming microorganism cultures as an example of Rayleigh-Taylor instability. *Nature*. 1974;248:441-3.
- [39] Papadaki A, Fernandes KV, Chatzifragkou A, Aguiéiras ECG, Da Silva JAC, Fernandez-Lafuente R, et al. Bioprocess development for biolubricant production using microbial oil derived via fermentation from confectionery industry wastes. *Bioresource Technology*. 2018;267:311-8.
- [40] Narayana Sarma R, Vinu R. Current status and future prospects of biolubricants: properties and applications. *Lubricants*. 2022;10:70.
- [41] Arumugam S, Sriram G. Effect of bio-lubricant and biodiesel-contaminated lubricant on tribological behavior of cylinder liner–piston ring combination. *Tribology Transactions*. 2012;55:438-45.
- [42] Nagendramma P, Kumar P. Eco-friendly multipurpose lubricating greases from vegetable residual oils. *Lubricants*. 2015;3:628-36.
- [43] Koriko OK, Shah NA, Saleem S, Chung JD, Omowaye AJ, Oreyeni T. Exploration of bioconvection flow of MHD thixotropic nanofluid past a vertical surface coexisting with both nanoparticles and gyrotactic microorganisms. *Scientific Reports*. 2021;11:16627.
- [44] Acharya N, Bag R, Kundu PK. Unsteady bioconvective squeezing flow with higher-order chemical reaction and second-order slip effects. *Heat Transfer*. 2021;50:5538-62.
- [45] Shamshuddin M, Mishra S, Kadir A, Bég OA. Unsteady chemo-tribological squeezing flow of magnetized bioconvection lubricants: numerical study. *Journal of Nanofluids*. 2019;8:407-19.
- [46] Zeeshan A, Arain M, Bhatti M, Alzahrani F, Bég OA. Radiative bioconvection nanofluid squeezing flow between rotating circular plates: Semi-numerical study with the DTM-Padé approach. *Modern Physics Letters B*. 2022;36:2150552.
- [47] Srinivasacharya D, Sreenath I. Bioconvection in a squeezing flow of a micropolar fluid in a horizontal channel. *Heat Transfer—Asian Research*. 2019;48:2155-73.
- [48] Yasmin, H., Bossly, R., Alduais, F.S., Al-Bossly, A. and Saeed, A., 2025. Thermally radiative water-based hybrid nanofluid with nanoparticles and gyrotactic microorganisms past a stretching surface with convective conditions and porous media. *Case Studies in Thermal Engineering*, 65, p.105644.

- [49] Chen Y, Renner P, Liang H. A review of current understanding in tribochemical reactions involving lubricant additives. *Friction*. 2023;11:489-512.
- [50] Adesanya SO, Ogunseye HA, Jangili S. Unsteady squeezing flow of a radiative Eyring-Powell fluid channel flow with chemical reactions. *International Journal of Thermal Sciences*. 2018;125:440-7.
- [51] He F, Wang Z, Wang L, Li J, Wang J. Effects of surfactant on capillary evaporation process with thick films. *International Journal of Heat and Mass Transfer*. 2015;88:406-10.
- [52] Fang T, Jing W. Flow, heat, and species transfer over a stretching plate considering coupled Stefan blowing effects from species transfer. *Communications in Nonlinear Science and Numerical Simulation*. 2014;19:3086-97.
- [53] Hamid RA, Nazar R, Pop I. Stagnation point flow, heat transfer and species transfer over a shrinking sheet with coupled stefan blowing effects from species transfer. *AIP Conference Proceedings: AIP Publishing*; 2016.
- [54] Raees A, Xu H, Liao S-J. Unsteady mixed nano-bioconvection flow in a horizontal channel with its upper plate expanding or contracting. *International Journal of Heat and Mass Transfer*. 2015;86:174-82.
- [55] Zhao Q, Xu H, Tao L. Unsteady bioconvection squeezing flow in a horizontal channel with chemical reaction and magnetic field effects. *Mathematical Problems in Engineering*. 2017;2017:2541413.